LLE Review

Quarterly Report

January – March 1983

LLE Review

Quarterly Report

Editor: R. S. Craxton
(716-275-5467)

January – March 1983

UR
LLE

IN BRIEF

This edition of the LLE Review contains articles on coronal-physics experiments on GDL and OMEGA, advances in x-ray diagnostics, the damage-testing and biological x-ray-diffraction facilities on GDL, progress in target fabrication, and NLUF experiments performed on OMEGA during the second quarter of fiscal year 1983 (January-March 1983). The following are some of the highlights of the work described in this issue:

- Work has continued on harmonic emission from GDL and OMEGA. A systematic study of spectral features of emissions at multiples of half the laser frequency has led to an improved understanding of these emissions as potential underdense-plasma diagnostics.

- Theoretical progress has been made on understanding the two-plasmon-decay instability. This complements the above-mentioned experimental work, since the plasma waves produced by this instability are responsible for many of the harmonic emissions. It has been shown that the spectrum of the most unstable modes depends strongly on the laser wavelength; also, reduced thresholds have been found for non-normal incidence.

- Two x-ray instruments incorporating free-standing x-ray transmission gratings have been developed. They are a spectrally dispersive microscope, used to obtain two-dimensional monochromatic images of laser-fusion targets,

and a transmission-grating streak spectrograph which allows for the simultaneous temporal and spectral resolution of target x-ray emission.

● Three additional developments in x-ray diagnostics are reported: high energy (12–14 keV) ionic spectral lines have been recorded with a Von-Hamos spectrograph, mosaic crystals have been used in a geometry which permits both high sensitivity and resolution, and two-dimensional imaging of 10-μm resolution has been achieved using Laue diffraction.

● Improvements have been made to the laser-driven x-ray-diffraction facility on GDL, and results have been obtained on time-resolved x-ray diffraction from photostimulated biological systems.

● An experimental system has been developed to better characterize the damage process in thin-film coatings. The crucial role played by impurities of sub-micron size has been established.

● New techniques have been developed for fabricating laser-fusion targets with ablation layers containing varying amounts of high-atomic-number material. Two polymeric materials and two coating techniques have been investigated.

● A computer-based system has been developed for the collection and reduction of visible spectroscopic data, permitting a turnaround time of a few seconds rather than several hours. This system was used in the harmonic-emission experiments on OMEGA.

● Spectra have been recorded of several high-Z ions in an NLUF experiment, and several new atomic levels have been identified.

CONTENTS

Bill Lockman, operator of the Glass Development Laser, adjusting the pinhole of one of the vacuum spatial filters. Accurate alignment of the laser beam through these pinholes is crucial for obtaining good beam quality.

Section 1
LASER SYSTEM REPORT

1.A GDL Facility Report

GDL continued operations this quarter as a 0.35-μm irradiation facility. Shots were taken into the BETA chamber in support of various interaction-physics, shell-hydrodymanics, and thermal-transport experiments. Damage testing continued with increased activity from the previous quarter. Several shots were directed into the x-ray chamber for x-ray-diffraction, biological-stimulation experiments, and for an NLUF experiment for the Naval Research Laboratory.

A total of 336 shots was delivered by the facility during the period January 1 to March 31, 1983. The shot distribution was as follows:

3ω Target Experiments	85	(25%)
Damage Test Facility	102	(30%)
X-Ray Chamber	60	(18%)
Miscellaneous	89	(27%)
TOTAL	336	(100%)

The 3ω target experiments were carried out in the BETA chamber and included interaction-physics, shell-hydrodynamics, thermal-transport, and Users' experiments.

1.B OMEGA Facility Report

OMEGA activities during this quarter have included the conclusion of the coronal-physics campaign, the x-ray-backlighting campaign, a limited NLUF campaign for the Naval Research Laboratory, reconfiguration of the system to provide 50-ps pulses for the x-ray-laser campaign, and initial manufacturing engineering necessary for the conversion of six OMEGA beams to the "blue" (0.35 μm).

Pulse-width stability, system reliability, and operations flexibility were highlights of the experimental campaigns. Due to the variety of programs, more time than usual was spent configuring diagnostics and preparing the laser system for shots; this prevented us from implementing substantial changes in the systems. Even though little time was available for maintenance, a near-perfect shooting record was achieved with minimal failures, and absolutely no shot days were lost due to equipment problems. One of the outgrowths of the coronal-physics campaign was the activation and successful calibration of several new diagnostics, including various x-ray spectrometers and visible-light spectrometers. We also made our first recording of backlit implosions during the x-ray-backlighting campaign; this work will be reported at a later date.

During a shutdown period consisting of the last two weeks of March, the oscillator was reconfigured to provide stable 50-ps laser pulses, and a minimal amount of system maintenance was carried out to allow for another quarter of operation prior to the June 3 shutdown planned for Blue Conversion.

Virtually every member of the operations group has been given an engineering assignment related to the Blue Conversion program. Through this quarter, the execution of these assignments has resulted in the specification, evaluation, and procurement of the main components of the conversion system, scheduling, and some component design and prototyping.

The distribution of OMEGA system shots during the period January 1 to March 31, 1983, was as follows:

Target Shots	123	(58%)
Beam Balance and Calibration	11	(5%)
Driver Alignment and Testing	49	(23%)
Miscellaneous	31	(14%)
TOTAL	214	(100%)

Section 2
PROGRESS IN LASER FUSION

2.A Harmonic Radiation from IR- and UV-Laser Plasmas

In order to optimize the coupling of laser light to laser-fusion targets, it is necessary to understand the basic laser-plasma interaction processes taking place in the plasma corona at densities up to the critical density. There the electron plasma frequency, ω_p, equals the laser frequency, ω_o, thus shielding the target interior from laser irradiation. All interaction processes depend to varying degrees on coronal parameters such as density, density gradients, coronal electron temperature, and plasma flow velocity. Thus, there is a premium on coronal diagnostics as well as on direct or indirect experimental signatures of the individual interaction processes.

A number of these interaction processes take place at or near the critical density (resonance absorption, parametric-decay instability) or the quarter-critical density [absolute Raman instability (SRS) and two-plasmon ($2\omega_p$) instability]. These processes typically involve the generation of one or more plasma waves with frequencies close to either ω_o (at n_c) or $\omega_o/2$ (at $n_c/4$). These plasma waves ("plasmons") can reradiate electromagnetic (e-m) waves in various ways, either through a combination of one, two, or more plasmons, or through scattering of incident photons from these plasma waves. The frequencies of the e-m waves generated in this way are typically multiples of half the laser frequency. Thus, many of the primary interaction processes can be diagnosed through the observation of the harmonic radiation emitted by the

3

plasma. Moreover, this radiation contains spectral details which relate to the coronal plasma conditions in the case of the odd-integer half-harmonics, while details of primary and secondary decay processes near n_c may be studied in the harmonics of the fundamental laser frequency.
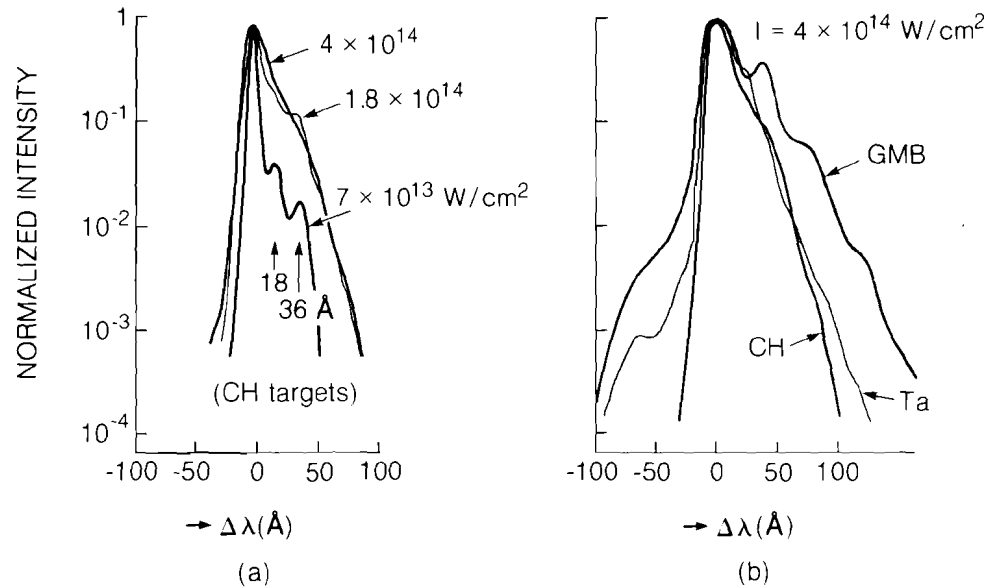
Thus, the interest in studying harmonic radiation from laser plasmas is twofold: we gain information on the laser-plasma interaction processes as well as on the plasma conditions in the interaction region. Furthermore, detailed understanding of these processes can shape and significantly influence future laser-plasma and laser-fusion experiments.

Over the past two years, we have investigated a number of laser-plasma interaction processes in UV- and IR-laser plasmas. We have observed a number of half-harmonics of the laser frequency, such as $\omega_o/2$, $3\omega_o/2$, $2\omega_o$, and $5\omega_o/2$. Not all harmonics could be observed under all irradiation conditions; in the UV experiments no spectra beyond the $3\omega_o/2$ harmonic were examined, while in the IR experiments the $\omega_o/2$ harmonic was only poorly resolved due to instrumental difficulties in this wavelength regime (2μm).

Harmonics of the fundamental irradiation frequency have been observed in laser plasmas for a long time.[1] The longer the irradiation wavelength, the higher the harmonics that have been observed.[2] In 1-μm irradiation the second harmonic is the principal integer harmonic observed. An excellent survey on second-harmonic generation and the underlying laser-plasma interaction processes has been published by Basov et al.[3] Two laser-plasma interaction processes are primarily responsible for the emission of multiples of the fundamental frequency, in particular the second harmonic. The first process, resonance absorption, involves linear conversion of incident photons into plasmons at n_c. This process does not have a threshold and is more efficient for obliquely incident p-polarized light than for s-polarized light.[4] The second process, the parametric-decay instability, occurs just below n_c; the incident e-m wave decays into a plasma wave and an ion-acoustic wave whose k-vectors are approximately parallel to the E-vector of the e-m wave, i.e., normal to the density gradient. Typical thresholds for this instability lie just below 10^{14} W/cm^2 for long-pulse (ns) IR irradiation. Evidence for this instability has been described in Refs. 3 and 5.

Second-Harmonic Spectra

Second-harmonic spectra obtained from OMEGA experiments (with $\lambda_L = 1.05\,\mu$m) have shown more details than hitherto reported (see Fig. 1). The reason for this greater spectral clarity is probably related to OMEGA's high degree of irradiation uniformity ($\lesssim 10\%$ rms variation) which surpasses that of earlier experiments. We note that the second-harmonic spectra typically contain a main peak with subsidiary lower-intensity peaks spaced by approximately 19 Å from each other to the red side of the main peak.

E2537

Fig. 1
Second-harmonic spectra from IR-laser plasmas. Spherical targets of various materials were irradiated in OMEGA with 24 beams for 1 ns at 1.05 μm. (a) Intensity dependence of spectra from solid CH spheres. (b) Target material (target-Z) dependence of spectra obtained by irradiating massive spherical targets at 10^{14} W/cm².
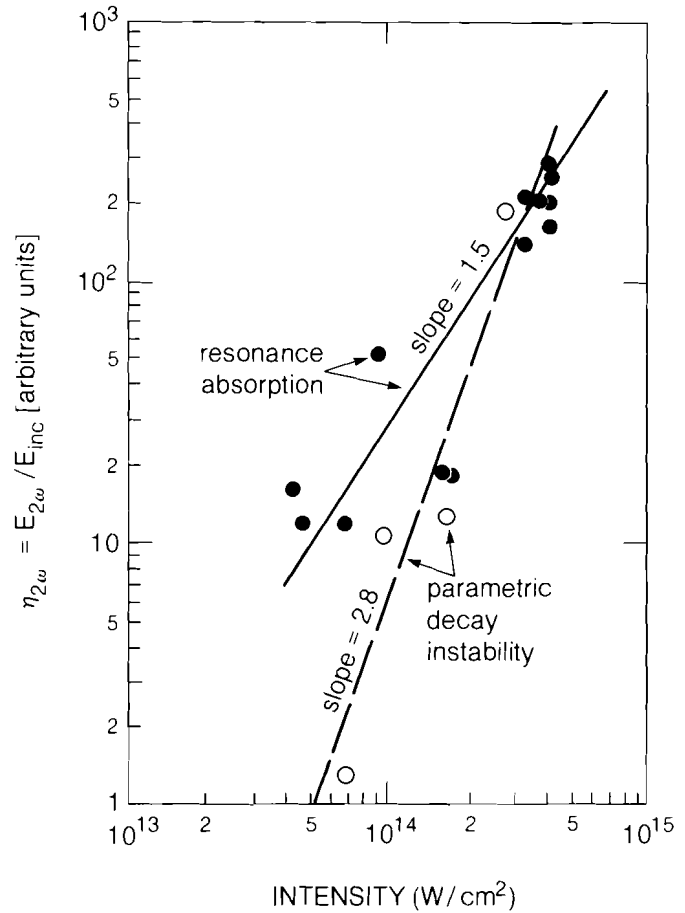
The main peak is traditionally identified with the existence of resonance absorption at n_c. Second-harmonic photons can be produced either by scattering of incident photons from the plasmons produced by resonance absorption or by two-plasmon-to-photon reconversion. From the polarization of this second-harmonic emission, we believe that scattering is the more likely process. The dependence of the 2ω emission on angle of incidence and polarization (p or s with respect to the plane of incidence) has led to clear identification of this spectral feature as a signature of resonance absorption. The intensity dependence of this spectral feature is expected to be

$$I_{2\omega}^{RA} \propto I_{\omega}^2 \text{, or } \eta_{2\omega}^{RA} \equiv I_{2\omega} / I_{\omega} \propto I_{\omega} .$$

In Fig. 2 we have plotted the experimentally observed intensity scaling of the main peak of the 2ω radiation relative to the incident radiation. The observed scaling is stronger than expected. This discrepancy may be explained by the intensity dependence of inverse-bremsstrahlung absorption: at lower intensities where the absorption is high the intensity at critical is substantially reduced from the incident intensity. Estimates of this effect have shown that the observed scaling is easily explained in this way.

The locations of the peaks on the red side of the main 2ω peak in Fig. 1 are apparently independent of either intensity (and therefore temperature) or target material (target Z). Furthermore, these side peaks are only seen above a certain irradiation intensity

Fig. 2
Intensity dependence of the main 2ω peak (solid circles) and the first red side peak (open circles). The main peak is due to scattering of incident photons on plasmons created by resonance absorption at n_c. The intensity scaling (solid line) is faster than expected due to the intensity dependence of inverse-bremsstrahlung absorption. The intensity of the side peak (dashed line) shows the predicted intensity behavior[3] of the parameteric-decay instability if the intensity dependence of inverse-bremsstrahlung absorption is taken into account.

($I \geq 5 \times 10^{13}$ W /cm²). Their intensities relative to the main 2ω peak rise with increasing irradiation intensity (see Fig. 2),

$$I_{2\omega}^{PD} / I_\omega \propto I_\omega^{2.8},$$

in close agreement with predictions made in Ref. 3 if allowance is made for the nonlinearly increased laser intensity at critical due to the intensity dependence of inverse-bremsstrahlung absorption. The generation of this radiation involves the combination of two plasmons generated by the parametric-decay instability just below n_c. At intensities above 4×10^{14} W /cm² the detailed structure of these side peaks merges into a continuum and saturates below the level of the main 2ω peak. In some cases, similar side peaks are found on the blue side of the main 2ω peak, though their intensities are approximately one order of magnitude below those of the red peaks. The peaks on the blue side are most easily seen for glass targets although they have also been seen for other targets under certain conditions. The blue substructure reported here is

much more detailed than reported previously.[3] Existing theory does not explain these blue-shifted peaks, though their splitting of twice that of the red substructure would appear to point to a related mechanism.

Odd-Integer Half-Harmonic Spectra

Spectra of the $3\omega_0/2$ emission have been observed for a long time.[6] The reason for the occurrence of $3\omega_0/2$ emission and other odd-integer half-harmonics lies in the existence of laser-driven instabilities at $n_e = n_c/4$, where $\omega_p = \omega_0/2$. At this density, the incident wave may be subject to either of two resonant decay processes, the absolute stimulated-Raman-scattering instability (SRS) and/or the $2\omega_p$-decay instability. In the former, the incident e-m wave decays into a scattered e-m wave and a plasma wave, both of frequency $\omega_s \approx \omega_p \approx \omega_0/2$, while in the $2\omega_p$-decay instability the incident e-m wave decays into two plasma waves with $\omega_p \approx \omega_0/2$. Due to the energy, momentum, and dispersion relations [Eq. (1)] the exact frequencies differ slightly from $\omega_0/2$, and the directions of the daughter waves also depend on the exact process involved as well as on the laser intensity. The wave-matching conditions and dispersion relations are given by:
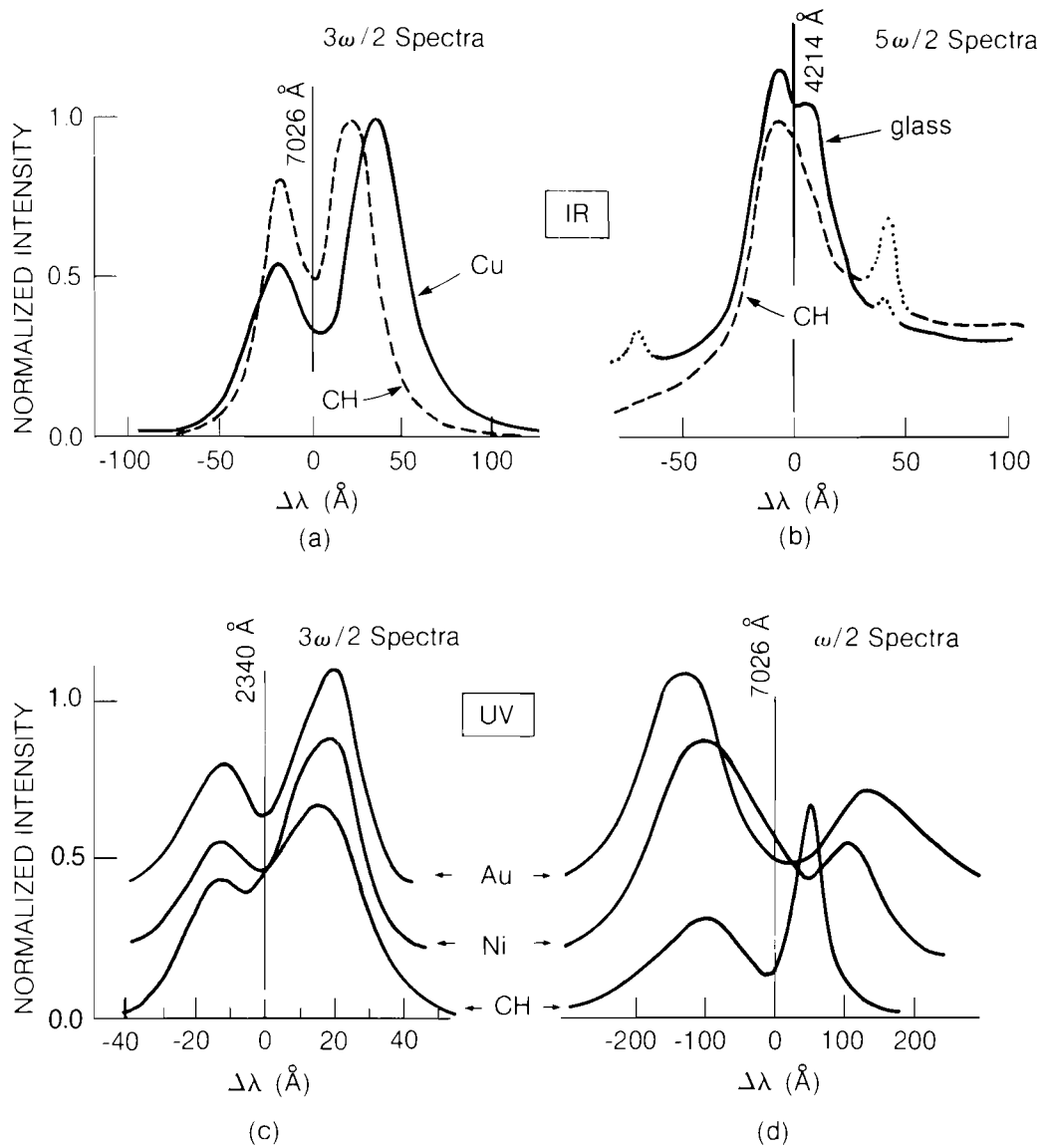
$$\omega_0 = \omega_{p1} + \omega_{p2}$$
$$k_0 = k_{p1} + k_{p2}$$
$$\omega_0^2 = \omega_{pe}^2 + c^2 k_0^2 \tag{1}$$
$$\omega_p^2 = \omega_{pe}^2 + 3v_T^2 k_p^2 \, ,$$

where ω_{pe} is the electron plasma frequency and v_T $(=\sqrt{kT_e/m_e})$ is the electron thermal velocity.

Typical odd-integer half-harmonic spectra are shown in Fig. 3. All of these spectra are generated by processes involving at least one of the plasmons generated at quarter critical. Typically, the $2\omega_p$ instability has the lower threshold and furnishes the plasmons required. The generation of these harmonics at quarter critical could be due to conversion of one, three, or five plasmons to photons, Thomson scattering of incident laser light from the same plasmons (for $\omega_0/2$ and $3\omega_0/2$ emission), or Thomson scattering of 2ω photons produced at critical.

The splitting of the spectral lines observed at all odd-integer half-harmonics is due to the two plasma waves generated at $n_c/4$ with frequencies just above and below $\omega_0/2$. The frequency difference is proportional to the coronal electron temperature and also depends on the k-vectors of the plasma waves. If the emission processes for $\omega_0/2$, $3\omega_0/2$, and $5\omega_0/2$ do not involve specific selections of plasma k-vectors, we may assume the splitting reflects the region of maximum growth of the $2\omega_p$-decay instability.[7] Then $\Delta\omega$ is proportional to $T_e f(k_{opt})$, where k_{opt} is the plasma wave vector corresponding to the optimum growth rate of the instability and $f(k) = [1 + 4(k/k_0)^2]^{1/2}$.

Radiation at $\omega_0/2$ can be produced either by SRS at $n_c/4$ or by linear reconversion of $2\omega_p$-decay plasmons into photons in a

Fig. 3
Odd-integer half-harmonic emission
from IR- and UV-laser plasmas.
(a) and (b): $3\omega_0/2$ and $5\omega_0/2$ spectra
from targets irradiated in OMEGA at
1 ns, 1.05 μm, and 4×10^{14} W/cm^2.
(c) and (d): $3\omega_0/2$ and $\omega_0/2$ spectra
obtained from targets irradiated in
GDL at 0.5 ns, 0.35 μm, and
4×10^{14} W/cm^2.

process which may be termed inverse resonance absorption. The former mechanism gives rise to a single red-shifted spectral component while the latter can give rise to red and blue components. In either case, the radiation should be polarized parallel to the incident laser light. The observed random polarization leads to the hypothesis that either the plasmons are scattered (randomized) prior to reconversion, or the $\omega_0/2$ photons are scattered after creation in such a manner as will destroy their polarization. The former process appears more likely as it is also required to allow the lower-frequency plasma waves to reach their critical density or turning point where the reconversion can take

place. The angular emission pattern for this process depends strongly on the density-gradient scale length at $n_c/4$. For typical UV experiments with scale lengths of about 50 μm, this implies that only plasmons with very small $k_\perp$ can be converted.

Alternatively, filamentation of the laser beam inside the plasma may be invoked, opening another way of producing $\omega_0/2$ radiation. The random polarization would then be a consequence of the steep radial density gradients inside the filaments. Angular emission patterns for this radiation have indeed shown indications of filamentation. However, while filamentation can easily explain the generation of the red component of the $\omega_0/2$ spectrum, the generation of the blue peak presents difficulties.

The interpretation of the intensity scaling of the frequency splitting of the $\omega_0/2$ spectra (Fig. 4) also presents a considerable challenge. The observed splitting is roughly proportional to the incident UV intensity, whereas we would expect it to be proportional to the coronal temperature, implying an approximate cube-root intensity scaling. Perhaps larger-angle plasmon scattering becomes more effective at higher intensities, thus allowing the inverse-resonance-absorption process to tap plasmons in different parts of the plasmon distribution depending on the incident intensity.

The $3\omega_0/2$-harmonic emission could be produced either by 3-plasmon conversion or by Thomson scattering of incident laser photons from $2\omega_p$-decay plasmons. We would expect the former process to lead to unpolarized emission, as in the case of the $\omega_0/2$ conversion. However, this is contrary to what has been observed; furthermore, it appears unlikely that the clear, double-peaked spectrum seen in Figs. 3a and 3c would be observed in this case.
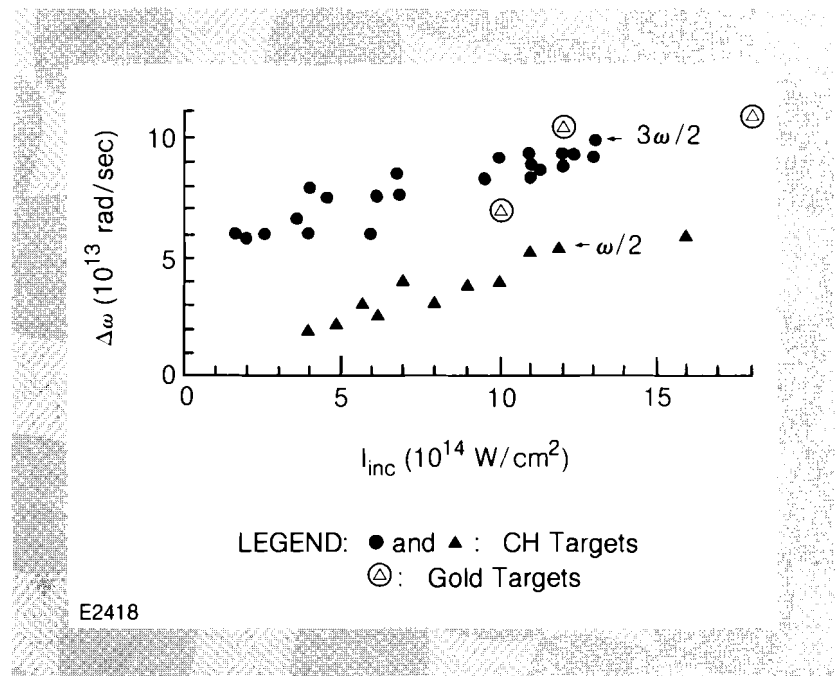

LEGEND: ● and ▲ : CH Targets
⊘ : Gold Targets

E2418

Fig. 4
Frequency splitting of the 1/2- and 3/2-harmonic spectra from UV-laser plasmas.

In contrast, the Thomson-scattering process preserves the polarization of the incident photons, but the random nature of the scattered $2\omega_p$-decay plasmons would lead to in-plane and out-of-plane scattering. This is indeed what we observe.

While the $3\omega_o/2$-harmonic splitting in IR experiments exhibits the expected double-peaked spectra symmetrically split around $3\omega_o/2$, the UV experiments show distinctly asymmetrical splitting (see Fig. 3c). Such asymmetry cannot be explained by existing theories at normal incidence. However, at oblique incidence such asymmetry may occur. Recent theoretical work at LLE indicates that the $2\omega_p$-decay instability may indeed occur with decreased thresholds inside self-focusing filaments which represent an extreme case of oblique incidence (90° with respect to the density gradient). This configuration would also eliminate a difficulty encountered in the k-matching conditions for the $3\omega_o/2$ scattering process in planar geometry for our UV experiments. This problem is related to the small plasma k-vector components perpendicular to the density gradient which have recently been predicted by Simon et al.[7] For typical IR-laser-plasma experiments Ref. 7 predicts $k_\perp$'s such that the 3 /2-harmonic radiation may be easily produced under most planar irradiation conditions without recourse to filamentation.

Comparing the theoretically predicted $3\omega_o/2$ spectral splitting to that measured experimentally in UV- and IR-laser plasmas (Fig. 5), we note a very close agreement under IR-irradiation conditions while the agreement is much less close for UV irradiation. The latter may be a result of our plotting average intensities, since from other experimental evidence we know that the $2\omega_p$-decay instability occurs predominantly in the hot spots of the irradiated area. Thus, an arbitrary shift in the experimental intensity scale by a factor of 4-5 to higher intensities would resolve the discrepancy. On the other hand, the predicted spectra should be symmetrical around $3\omega_o/2$ which they are not. The resolution of these problems may involve filamentation: preliminary calculations of $3\omega_o/2$ generation inside filaments suggest that this effect may explain both the asymmetry and the magnitude of the spectral splitting.

The $5\omega_o/2$ spectra observed in our IR-irradiation experiments on OMEGA have only been looked at in a cursory fashion. However, the frequency splittings of the $5\omega_o/2$ and $3\omega_o/2$ spectra in Fig. 3b are equal under equivalent experimental conditions, implying that the same plasma waves are involved in both processes. The $5\omega_o/2$ scattering process could be viewed as Thomson scattering of 2ω photons on $2\omega_p$-decay plasmons at $n_c/4$. The 2ω photons would be produced by resonance-absorption plasmons as described earlier. The low level of $5\omega_o/2$ radiation has precluded a systematic study to date, but its existence and generation mechanism appear well established. From images of spherically irradiated targets taken in $3\omega_o/2$ and $5\omega_o/2$ light, we have clearly established that the $5\omega_o/2$ radiation does indeed come from the $n_c/4$ surface.[8]
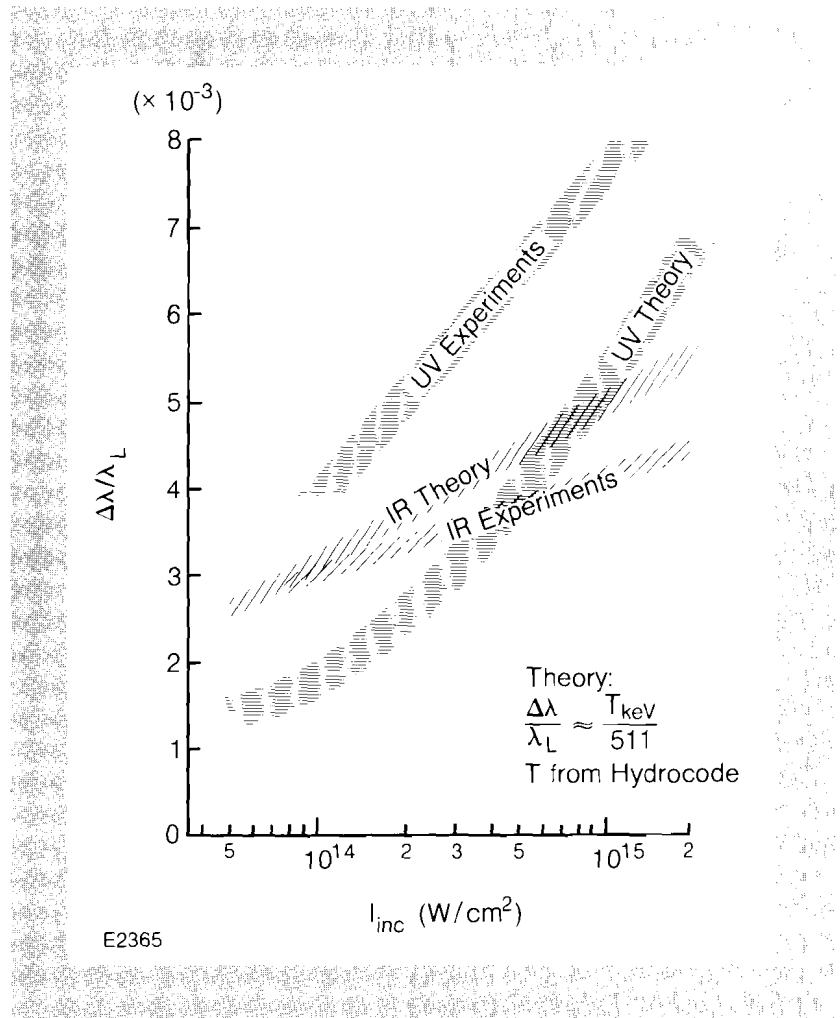
Fig. 5
Intensity dependence of the splitting of 3/2-harmonic spectra from IR- and UV-laser plasmas. The UV data were obtained from planar CH targets irradiated in GDL (λ_l = 0.35 μm, 0.5 ns). The IR data were obtained on OMEGA with 1-ns, 24-beam symmetrical irradiation of solid CH spheres. The theoretical curves are obtained from temperatures predicted by hydrodynamic simulations and the formula $\Delta\lambda/\lambda_l = T_{keV}/511$.

Conclusion

We have observed a multitude of harmonics from IR- and UV-laser plasmas. Their generation mechanisms are generally well understood within the framework of existing theories, although detailed analyses require at times sophisticated extensions to these theories. In the relatively uniform plasmas produced by the 24-beam, 1.05-μm OMEGA system the measured spectra are well matched by theoretical predictions. In the current UV experiments with their less uniform illumination the correlation with theory is not so close, particularly as regards the ω_0/2 spectra.

REFERENCES
1.   A. Caruso, A. deAngeles, G. Gratti, R. Gratton, and S. Martellucci, Phys. Lett. **33A**, 29 (1970).

2.   N. H. Burnett, H. A. Baldis, M. C. Richardson, and G. D. Enright, Appl. Phys. Lett. **31**, 172 (1977).

3.   N. G. Basov, V. Yu. Bychenkov, O. N. Krokhin, M. V. Osipov, A. A. Rupasov, V. P. Silin, G. V. Sklizkov, A. N. Starodub, V. T. Tikhonchuk, and A. S. Shikanov, Sov. Phys. JETP **49**, 1059 (1979).

4. K. R. Manes, V. C. Rupert, J. M. Auerbach, P. Lee, and J. E. Swain, *Phys. Rev. Lett.* **39**, 281 (1977).

5. C. Yamanaka, T. Yamanaka, T. Sasaki, J. Mizui, and H. B. Kang, *Phys. Rev. Lett.* **32**, 1038 (1974).

6. P. Lee, D. G. Giovanielli, R. P. Godwin, and G. H. McCall, *Appl. Phys. Lett.* **24**, 406 (1974).

7. A. Simon, R. W. Short, E. A. Williams, and T. Dewandre, submitted to *Phys. Fluids*.

8. J. Rizzo, S. Letzring, D. Villeneuve, M. C. Richardson, G. Gregory, R. S. Craxton, J. Delettrez, K. Lee, and R. Hutchison, Proceedings of the Second Conference on Lasers and Electro-Optics (CLEO), Phoenix, AZ (1982). See also LLE Review **13**, Section 2.C (1982).

2.B Advances in the Theory of the Two-Plasmon Decay Instability in an Inhomogeneous Plasma

We report recent calculations of the growth rate of the two-plasmon-decay $(2\omega_p)$ instability, in which we show that although previously published thresholds[1-3] are substantially correct, the spectrum of the most unstable modes depends strongly on the laser wavelength. In addition, we have found substantially reduced thresholds when the laser is incident at an oblique angle to the density gradient of the coronal plasma.

The presence of the strong electromagnetic wave of the laser in the corona of a laser-fusion target provides a source of free energy which can be tapped by a number of plasma instabilities. One example of these is the two-plasmon-decay instability in which the pump electromagnetic wave (the laser light) decays into two plasma waves. The pump wave and the two plasma waves have frequencies and wave vectors $(\omega_o, \mathbf{k}_o)$, $(\omega, \mathbf{k})$ and $(\omega_o - \omega, \mathbf{k}_o - \mathbf{k})$, respectively. The physical mechanism for instability is that the first plasma wave and the pump produce a ponderomotive force on the plasma at the beat (difference) frequency of $\omega_o - \omega$ which resonantly drives the second wave. In turn, the beating of the second wave with the pump at frequency $\omega_o - (\omega_o - \omega) = \omega$ resonantly drives the first wave. With sufficient coupling, that is, with a sufficiently strong pump, the positive feedback overcomes the losses due to damping and/or convection of the product waves out of the region, and instability occurs. The coupling mechanism is the same as that which gives rise to Brillouin and Raman scattering. The distinguishing feature of the the $2\omega_p$ instability is that both decay waves are plasma waves. The coupling is most effective when the plasma waves are resonantly driven, that is, when the product waves satisfy the free Langmuir dispersion relations:

$$\omega^2 = \omega_p^2 + 3v_T^2 k^2$$

and

$$(\omega_o - \omega)^2 = \omega_p^2 + 3v_T^2 (k_o - k)^2 \; , \tag{1}$$

where v_T is the electron thermal velocity and ω_p is the plasma frequency.

Because the thermal corrections are relatively small this requires

$$\omega \approx \omega_o - \omega \approx \omega_p \approx \omega_o /2 \; , \tag{2}$$

and so the instability occurs in the vicinity of the quarter-critical density. From Eq. (1) one can readily show that the difference between the frequencies of the two coupled waves is given by

$$\Delta \omega = \frac{6v_T^2}{\omega_o} \; k_o \cdot (k - k_o /2) .$$

The frequency splitting is thus proportional to the temperature of the plasma, and to a factor that depends on the k-vector of the unstable mode, which is undetermined at this point.

By various mechanisms such as Thomson scattering of the laser radiation or linear conversion, the plasma-wave spectrum from the $2\omega_p$ instability gives rise to radiation at half-odd-integer harmonics (HOIH), that is $\omega_o /2, 3\omega_o /2, 5\omega_o /2$, etc. One can thus hope to use this HOIH radiation as a temperature diagnostic if the relevant k-vectors are known. Indeed, as is described elsewhere in this issue (Section 2.A), multi-peaked HOIH spectra have been observed in both 1-μm and 0.35-μm experiments with splittings of various magnitudes.

Apart from its possible use as a diagnostic, the $2\omega_p$ instability is potentially important if it should absorb a substantial fraction of the laser light into plasma waves, which would in turn transfer this energy to the electrons by accelerating them to approximately their phase velocity. A substantial population of hot ($\sim$ 100 keV) electrons from this source would give rise to target-design problems because of the preheat that would be caused in the fuel. In our experiments to date, however, only small ($\lesssim 0.1\%$) hot-electron populations have been observed.[4]

The theory of the $2\omega_p$ instability in a homogeneous plasma was first worked out by Jackson,[5] who found that the most unstable modes have k-vectors lying in the plane of incidence on the hyperbola shown in Fig. 6. Each point of the hyperbola corresponds to a particular density determined by the frequency-matching conditions in Eq. (1). The homogeneous growth rate is independent of density until Landau damping becomes important. This occurs for $k\lambda_D \gtrsim (k\lambda_D)_{max} \equiv p \simeq 0.3$. In an inhomogeneous plasma, as arises in laser-fusion experiments, the $2\omega_p$ instability is excited in
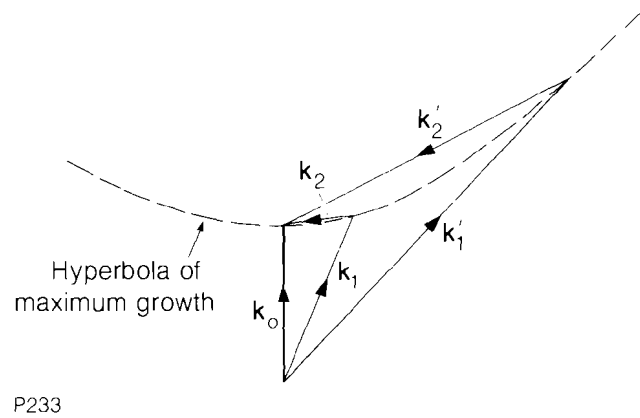
Fig. 6
Decay of photon (k_o) into two plasma waves (k_1, k_2) or (k_1', k_2'). In a homogeneous plasma, these decays are equally unstable. In an inhomogeneous plasma, $\beta << 1$ (as in CO_2 laser experiments) favors the primed decay and $\beta >> 1$ (as in short-wavelength experiments) favors the unprimed.

a small region of density just below quarter-critical, approximately in the range

$$1 - 3p^2 \, (\approx 0.18) < n \, / n_{c \, 4} < 1 - 9v_T^2 / 4c^2 \quad,$$

the lower limit arising from Landau damping and the upper from frequency matching. As the pump is increased, the instability is first convective, and plasma waves generated thermally (or otherwise) are amplified as they pass through the resonant region. On further increase of the pump the instability becomes absolute. The final level of the plasma-wave amplitudes is then limited only by nonlinear dissipation and not by convective loss from the resonance region, and is independent of the noise level from which the waves grew up.

The theory of the absolute $2\omega_p$ instability in an inhomogeneous plasma was first treated by Lee and Kaw,[1] who restricted their calculation to the case of plasma waves whose wave vector greatly exceeded that of the pump. A more complete theory which included all ranges of plasma-wave wave number was developed by Liu and Rosenbluth.[2] However, in the final stages of their calculation they resorted to various inappropriate approximations, which led to certain anomalies first pointed out by Lasinski and Langdon.[3] We have corrected and extended their calculations[6] to obtain growth rates and thresholds for the absolute $2\omega_p$ instability, for oblique as well as normal incidence of the pump. In the course of these calculations we have identified a new parameter of importance, namely β, defined by

$$\beta = 9v_T^4 \, k_o^2 \, / \, v_o^2 \omega_o^2 = 1.41 \, T_{keV}^2 \, / I_{14} \lambda_\mu^2 \quad,$$

where $v_o = eE \, / m\omega_o$ is the electron "jitter" velocity in the pump field, which provides a qualitative measure of the relative

importance of thermal effects and the effect of the pump on the dispersion of the plasma waves. Because the self-consistent variation of electron temperature T_{keV} (in units of keV) with pump power I_{14} (in units of 10^{14} W/cm^2) tends to cancel the explicit dependence of β on pump power, β is determined primarily by the vacuum laser wavelength λ_μ (in microns). Typically $\beta \ll 1$ for CO_2 laser experiments, while for 1-μm or shorter-wavelength laser experiments, $\beta \gtrsim 1$.

The threshold for absolute instability is found to be a relatively weak function of β given approximately by

$$\left(\frac{v_o}{v_e}\right)^2 k_o L > 3 \ ,$$

or $I_{14} L_\mu \lambda_\mu / T_{keV} > 60$ in practical units. However, the wave number of the most unstable mode is sensitive to p. The perpendicular component of this wave number $k_\perp$ is given approximately by

$$k_\perp \simeq 0.5 \, k_o \beta^{-\frac{1}{2}}.$$

The component of the wave number parallel to the gradient, $k_{||}$, is of course ill-defined because it is a function of position. However, the unstable eigenfunction has its maximum amplitude near the point where $k_{||}$ and $k_\perp$ are related by the hyperbola of Fig. 6, that is where

$$k_{||} (k_{||} - k_o) = k_\perp^2 \ .$$

Thus, when $\beta \ll 1$, $k_{||} \simeq k_\perp \gg k_o$, and the most strongly excited plasma waves make an angle of approximately 45° to the pump. This has been directly observed in the Thomson-scattering experiments of Baldis and Walsh[7] who used a CO_2 laser incident on a preformed plasma. In this case ($\beta \ll 1$), the dependence of $k_{||}$ on β cancels the v_T^2 dependence of $\Delta\omega$ in Eq. (2), and one obtains a frequency splitting given by

$$\Delta\omega / \omega_o = 2.24 \, v_o / c = 4.8 \times 10^{-3} \, \lambda_\mu I_{14}^{\frac{1}{2}}$$

for the fastest-growing mode. On the other hand, when $\beta \gtrsim 1$, the most unstable $2\omega_p$ mode is into a pair of plasma waves, one with wave vector approximately equal to that of the pump and the other with a wave vector smaller than the pump and approximately perpendicular to it. This second wave typically has a phase velocity greater than the velocity of light and should be relatively ineffective in accelerating electrons. The first wave, however, should generate hot electrons directed up the density gradient. Indications that this is the case arise from a comparison of hard-x-ray spectra and electron-spectrometer data.[8] When short-wavelength probe pulses become available at LLE, Thomson-scattering experiments will permit direct measurements of plasma-wave spectra, and verification of our theoretical conclusions in

this case will be possible. In this case ($\beta \ll 1$) one obtains a frequency splitting

$$\Delta\omega/\omega = (9/2)v_T^2/c^2 = 8.8 \times 10^{-3} \, T_e(keV)$$

corresponding to the fastest-growing mode $k \approx k_o$ in Eq. (2).

We have extended our calculations to the case of oblique incidence of the pump, and reached two important conclusions.[9] First, the threshold for two-plasmon decay is reduced by a factor of approximately $\cos\theta$, θ being the angle between the pump wave vector and the density gradient in the unstable region. This is the case for both s- and p-polarization. Second, in the case of p-polarization the growth rate is no longer a symmetric function of $k_\perp$: plasma waves with wave vectors more oblique to the gradient are found to be more unstable.

In summary, it has been found that for typical experimental parameters the expected decay-wave spectrum of the $2\omega_p$ instability depends on the laser wavelength. For long-wavelength (e.g., 10-μm) lasers, plasma waves with large wave vector are most unstable, while for shorter-wavelength ($\leq 1\mu$m) lasers the opposite is the case. In addition, when the laser is obliquely incident, lower thresholds are expected, and in the case of p-polarization asymmetric plasma-wave spectra are produced.

REFERENCES

1. Y. C. Lee and P. W. Kaw, *Phys. Rev. Lett.* **32**, 135 (1974).

2. C. S. Liu and M. N. Rosenbluth, *Phys. Fluids* **19**, 967 (1976).

3. B. F. Lasinski and A. B. Langdon, Lawrence Livermore 1977 Annual Report UCRL-50021-77.

4. LLE Review **13**, Section 2.D (1982).

5. E. A. Jackson, *Phys. Rev.* **153**, 235 (1967).

6. A. Simon, R. W. Short, E. A. Williams, and T. Dewandre, submitted to *Phys. Fluids*.

7. H. A. Baldis and C. J. Walsh, *Phys. Fluids* **26**, 1364 (1983).

8. D. M. Villeneuve, R. L. Keck, B. B. Afeyan, W. Seka, and E. A. Williams (to be published).

9. B. B. Afeyan, E. A. Williams, R. W. Short, and A. Simon, *Bull. Am. Phys. Soc.* **27**, 951 (1982).

2.C Broadband Spectrally Resolving X-Ray Instrumentation

The examination of the spectral characteristics of x-ray emission from high-density plasmas has long been utilized as an effective diagnostic of the plasma state. The diagnosis of laser-produced plasmas makes special requirements of x-ray spectroscopic techniques in that extremes of temperature and density are created within microscopic regions and evolve in time on an ultrafast

timescale. There is currently a strong interest in such plasmas, notably because of their utilization in various laser-fusion and x-ray-laser schemes, but also because of a more general need to understand the rich variety of interaction mechanisms possible in such plasmas. In addition, laser-produced plasmas show considerable potential as ultrashort, high-fluence x-ray sources, suitable for a wide variety of applications such as x-ray flash radiography, kinetic x-ray diffraction, and x-ray absorption spectroscopy.

In general, such studies would be better served by experimental diagnostic techniques which, in addition to spectral resolution, provide spatial discrimination of the origin of the x-ray emission and the capacity to delineate in time its spectral and spatial features. These requirements are nowhere more necessary than in the study of laser-fusion plasmas, where spectrally resolved data in the 0.1–50-keV range is required along with micron spatial accuracy and picosecond temporal resolution.[1]

We describe here in detail two x-ray instruments incorporating free-standing x-ray transmission gratings to provide broadband spectral resolution. The first, a spectrally dispersive microscope, may be used to obtain two-dimensional monochromatic spatial images of laser-fusion targets. This instrument has been used to measure the spatial extent of the core of an imploded glass microballoon containing a mixture of deuterium and argon, as reported in an earlier issue of the LLE Review.[2] The second instrument, a transmission-grating streak spectrograph, allows for the simultaneous temporal and spectral resolution of target x-ray emission.

Spectrally Dispersive Microscope

Line-specific dispersed images can be produced with the incorporation of a low-dispersive-power element into the optical path of an x-ray microscope.[3] The most suitable element for this purpose is a free-standing x-ray transmission grating, which introduces negligible optical distortion, is inherently efficient, and is relatively easy to implement. Finely spaced metallic gratings having a spatial period of 300 nm (bar width 180 nm) have recently been developed with grating thicknesses of ~ 600 nm over large areal extents (~ 1 cm^2).[4] In collaboration with N. M. Ceglio of Lawrence Livermore National Laboratory, A. M. Hawryluk of MIT, and C. H. Hooper of the University of Florida, we have integrated such a grating into the optical path of a four-channel Kirkpatrick-Baez microscope. This instrument, shown in Fig. 7, utilizes an array of four cylindrical mirrors with radii of curvature 32.4 m, in a fixed-focus optically contacted array for greater stability. It has a total solid-angle acceptance of ~ 10^{-6} sr, producing a 5× magnified image 127 cm from the target with a spatial resolution of ~ 4 μm. The mirrors are Ni-coated, which in combination with Be and Al K-edge filters gives a spectral acceptance range of 1.5–4.5 keV under the assumption of a Boltzmann x-ray source function of temperature ~ 1 keV. The grating is deployed at a point along the viewing axes of the microscope, 20.3 cm from the mirror
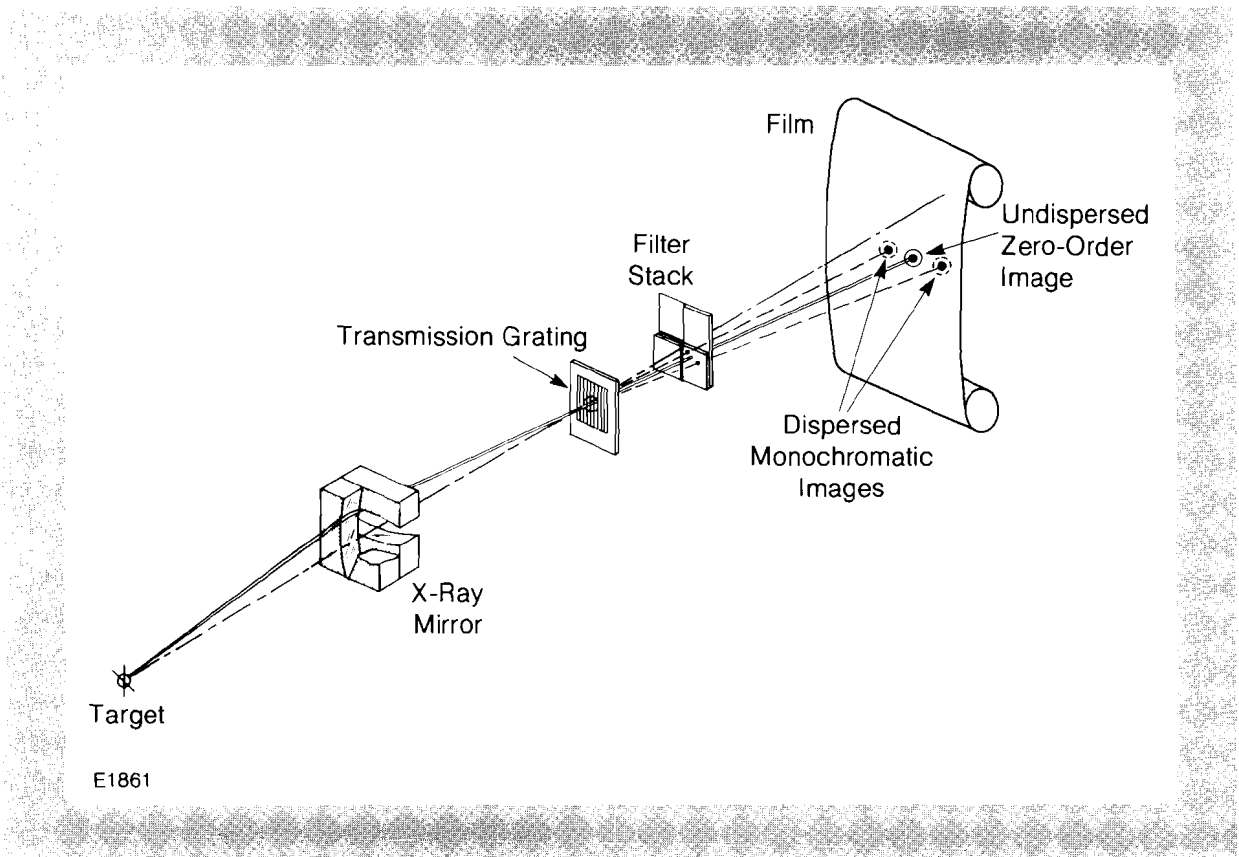
Fig. 7
Schematic of modified Kirkpatrick-Baez microscope. Four images of the target are formed on the film by crossed cylindrical grazing-incidence mirrors. Each image is dispersed spectrally in one direction by the transmission grating and may be selectively filtered in a filter stack.
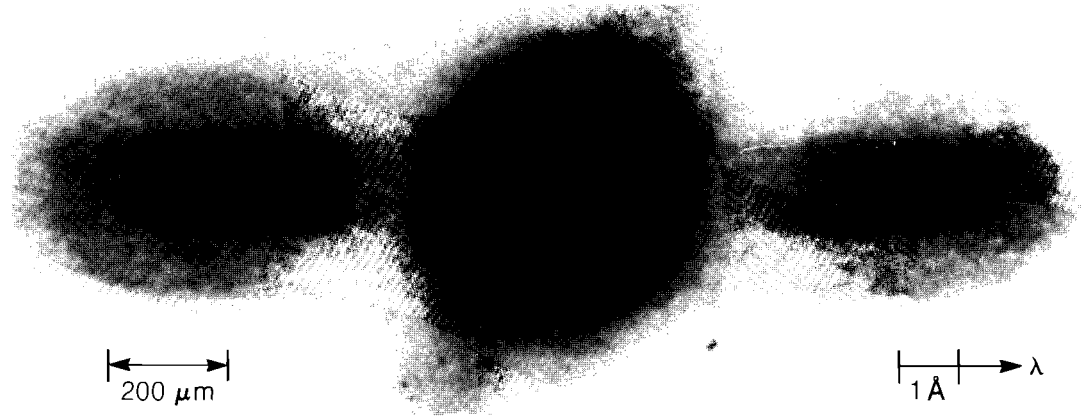
block, where the four microscope image axes intersect. With a distance of 78.7 cm to the image plane, this gives a dispersion of $d\lambda/ds \approx 3.75$ Å/mm, with an effective spectral resolution in the dispersion direction of $\sim$5 Å. The spatial resolution in the dispersion-free direction should not be significantly degraded by the imposition of the grating in the optical path.

A typical image from this instrument is reproduced in Fig. 8, showing a multiply dispersed image of a 540-μm-diameter, 1.0-μm-thick glass microballoom imploded by a 1-ns, 2-kJ pulse from the 1.05-μm, 24-beam OMEGA laser facility. The central, deliberately overexposed image is one of the four undiffracted (zeroth-order) images produced by the microscope. On either side of this image can be seen the first-order dispersed images of the imploded target. Clear images of the core and corona in emission from He-like and H-like Si and Ca can be determined in the $\sim$ 6-Å range. High-resolution spectrally specific imaging of this type has already proved valuable to the analysis of imploded target cores,[2] and is expected to be of considerable importance for studies of the stability of imploding shells and for the analysis of two-dimensional features of energy transport and ablation.

Transmission-Grating Streak Spectrograph

Transmission diffraction gratings of the type described above may be deployed in ideal, low-dispersion, broadband spectrographs of high efficiency. In conjunction with an x-ray streak
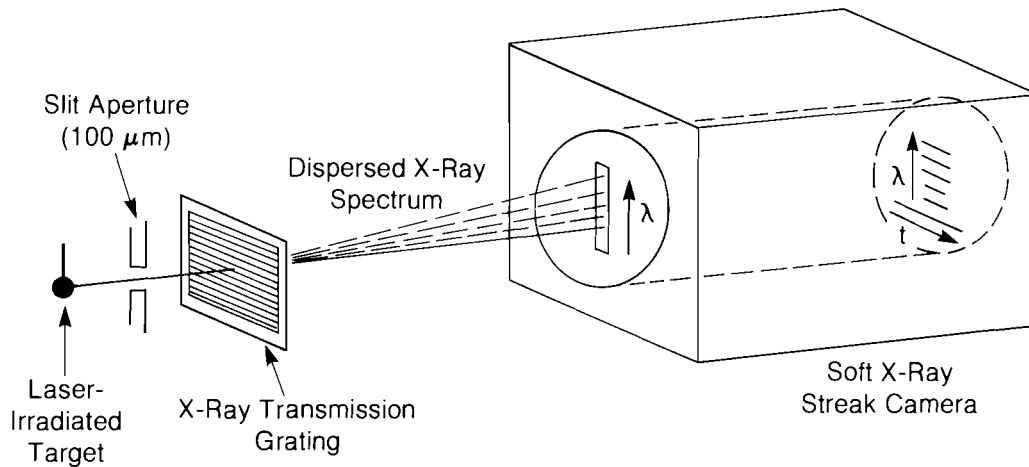
camera, a high-time-resolution spectrograph is created.[5] In the device constructed at LLE, shown schematically in Fig. 9, a transmission diffraction grating similar to the one described above is mounted together with a 150-μm slit aperture in the path between the target and the streak camera. The x-ray emission from the laser-irradiated target is dispersed along the admittance

200 μm

1 Å ⟶ λ

E2160

Fig. 8
Dispersed image of a 540-μm-diameter glass microballoon of wall thickness 1μm, imploded by the OMEGA laser system. The undiffracted (zeroth-order) x rays form a conventional image, overexposed here; first order images are formed from different spectral components diffracted from the zeroth-order image by the transmission grating.

Slit Aperture
(100 μm)

Dispersed X-Ray
Spectrum

λ

λ

t

Laser-
Irradiated
Target

X-Ray Transmission
Grating

Soft X-Ray
Streak Camera

E1863

Fig. 9
Transmission-grating x-ray streak spectrograph. X rays from the target pass through a slit aperture and transmission grating and are dispersed spectrally along the photocathode of the streak camera, which subsequently disperses the spectrum in time. The film record produced represents x-ray intensity as a function of wavelength and time.

slit of the streak camera, which subsequently disperses the spectrum in time.

The streak camera employs a photocathode which consists of 10 nm of gold evaporated onto a 1.5-μm-thick stretched polypropylene substrate. The polyimide substrate of the transmission grating blocks most x rays less energetic than 500 eV. The efficiency of the grating in diffracting x rays more energetic than 500 eV is about 0.1. X rays that pass undiffracted form the zeroth order, from which position the distance of dispersion along the photocathode is proportional to wavelength. The ability of the device to resolve higher-energy x rays, only slightly dispersed in the first order, from the zeroth-order diffraction imposes an upper energy of $\sim$ 10 keV on the dispersed spectrum.

The spectral resolution and dispersion can easily be determined. The grating and slit are placed together, at a distance L = 108 cm from the target and at a distance D = 110 cm from the streak-camera photocathode. The slit width A is 150 μm, and the grid is d = 0.3 μm. Thus, the spectral resolution in m'th order ($\delta\lambda$), defined by the equation

$$\delta\lambda = \left[\frac{(S+A)}{L} + \frac{A}{D} \right] \frac{d}{m} ,$$

is $\approx$ 1.9 Å, for a target of source size S = 400 μm as is characteristic of the initial diameter of the spherical targets used in our experiments. The resolution is explicitly dependent on the extent of the emitting region; for sources smaller than about twice the slit-aperture size, the resolution approaches a limiting value of $\sim$ 0.8 Å. The spectral dispersion in the streak-camera plane, derived from the Bragg condition sin θ = mλ/d, is dλ/ds = d /mD $\approx$ 2.76 Å /mm. Thus the 1-cm-long photocathode includes all of the spectrum above the carbon K-edge passed by the polyimide substrate of the transmission grating. The temporal resolution of the streak camera is estimated to be $\sim$ 30 ps.

The large spectral range and good temporal resolution of this device, afforded by the high efficiency of the grating, compensate for the relatively low spectral resolution, and make the device particularly suitable for qualitative and comparative studies. This is illustrated in Fig. 10, which shows the time-resolved spectrum of the x rays emitted from a glass microballoon, of 594-μm diameter and 1.3-μm wall thickness, filled with 20 atm of DT. This was uniformly irradiated with a 1-ns pulse from the 24-beam OMEGA laser system, with a total energy of 2.8 kJ. The brightest time-smeared signal in Fig. 10 is that of the zeroth-order undispersed x-ray emission. However, emission in the first order at $\sim$ 6 Å, corresponding predominantly to resonance-line emission from Si in the glass shell, can be seen to persist throughout the irradiation of the target. At the stagnation of the implosion, the core temperature increases, giving rise to a brief, bright emission from the other line radiation, and x-ray continuum in the 1- to 20-Å range.

Summary

Two new diagnostics have been developed, illustrating the potential of spectrally discriminating space-resolved and time-resolved x-ray instrumentation to the diagnosis of laser-fusion target implosions. These and similar devices will prove valuable to the diagnosis of thermal transport in planar and spherical targets, and to the analysis of the final conditions within imploding spherical targets.
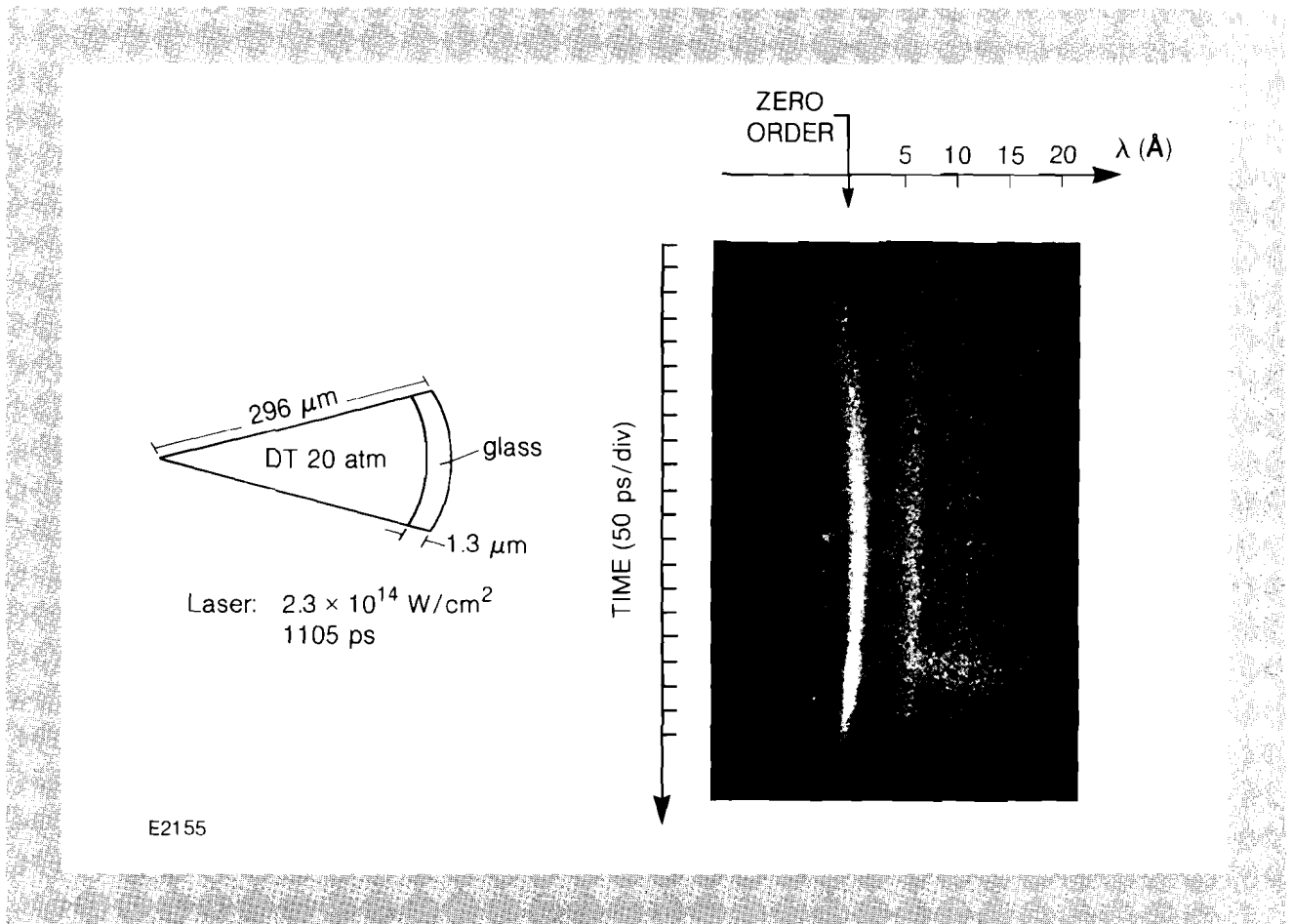

Fig. 10
.X-ray streak spectrograph record of a bare glass microballoon imploded by the OMEGA laser system. The undiffracted (zeroth-order) component lasts throughout the laser pulse. The prominent emission at about 6 Å is Si emission from target shell material; at relatively late times, a broad spectral feature marks the peak implosion of the target.

REFERENCES

1. D. T. Attwood, *IEEE J. Quantum Electron.* **QE-14,** 909 (1978).

2. LLE Review **12,** 12 (1982).

3. P. Kirkpatrick and A. V. Baez, *J. Opt. Soc. Am.* **38,** 766 (1948).

4. A. M. Hawryluk, N. M. Ceglio, R. H. Price, J. Melngailis, and H. I. Smith, *Proc. Topical Conf. Low Energy X-Ray Diagnostics,* AIP Conf. Proc. No. 75, p. 286 (1981).

5. N. M. Ceglio, R. L. Kauffman, A. M. Hawryluk, and H. Medici, LLNL Report UCRL-81800 (unpublished) (1982).

2.D X-Ray Crystal Devices: Diagnostic Developments

Laser-fusion experiments will involve ever-increasing compressed target densities, attained in regions of small spatial dimension. With fast-electron preheat minimized by the use of short-wavelength laser radiation, ablatively driven targets are expected to produce high-density imploded cores at relatively low temperatures. For diagnostic purposes, there is a clear need for x-ray devices of greater sensitivity and higher spatial resolution.

We report here three developments in x-ray diagnostics: (a) using a Von-Hamos x-ray spectrograph, we have obtained ionic spectral lines of higher energy (12–14 keV) than has been previously observed; (b) mosaic crystals have been used in a geometry which yields both high sensitivity and resolution; and (c) two-dimensional imaging of ~ 10-μm resolution has been achieved using Laue diffraction.

Von-Hamos Focusing Crystal Spectrography

The Von-Hamos x-ray spectrograph[1] consists of a cylindrically curved crystal whose axis normally lies in the plane of the recording film. The radiation source lies on this axis as well (see Fig. 11a). A wide-range spectrum is obtained on the film with a flux which is higher by a large factor than in the corresponding flat-crystal case. This factor, of the order of the ratio between the crystal radius of curvature and the source radius, can be several hundred for laser-fusion targets. In a preliminary study,[1] we demonstrated an increase by a factor >100 in the flux on film, by bending mica to a 5-cm radius of curvature and observing first-order diffraction of radiation from laser-irradiated targets. This increase in sensitivity is important for the diagnosis of high-density, low-temperature implosions. To realize the full potential of the instrument it is crucial to master the art of bending crystals to small radii of curvature. Considerable effort has been devoted to studying the properties of various crystals under bending, polishing, and abrading treatments; this is reported elsewhere.[2]

Figure 11 shows an example of focusing (imaging) using a mica crystal in fifth order. The source (Fig. 11b) was a steel mesh (50-μm bar width) fluorescing Fe K_α radiation when irradiated by copper K_α radiation from an x-ray tube. Spatial resolution of at least 50 μm is evident in Fig. 11c. Imaging in the up-down direction in the plane of Fig. 11c is entirely due to the Von-Hamos focusing. Imaging in the left-right, dispersion direction is due to the monochromaticity of the radiation source.

In order to demonstrate further the capabilities of the Von-Hamos spectrometer, we performed a small number of test shots on the 24-beam OMEGA laser system. In these shots, short pulses (100 ps) of high power ($\sim$ 6 TW) were used to explosively implode small targets (diameters 50–80 μm), in which high core temperatures of 3-4 keV were achieved. The unique capability of

the instrument is demonstrated by the observation of spectral lines from the compressed core of a shorter wavelength (0.95 Å) than any previously reported ionic lines (see Fig. 12). Furthermore, all spectra were so intense as to cause film saturation. We stripped the front emulsion of the (Kodak no-screen) film by a bleaching agent and the spectra shown in Fig. 12 were recorded on the back emulsion, being very intense even then.

These spectra were obtained with two curved crystals: LiF 200 (2d = 4.03 Å) and LiF 220 (2d = 2.85 Å). The Ge spectrum was obtained from imploding germania (GeO$_2$) shells of diameter 50 μm and thickness 0.7 μm. The Kr lines were obtained from a glass shell of diameter 57 μm and wall thickness 1.05 μm, filled with krypton at a pressure of 10 atm. To observe the higher-energy lines of the Kr^{+34} spectrum, a different crystal would be required.
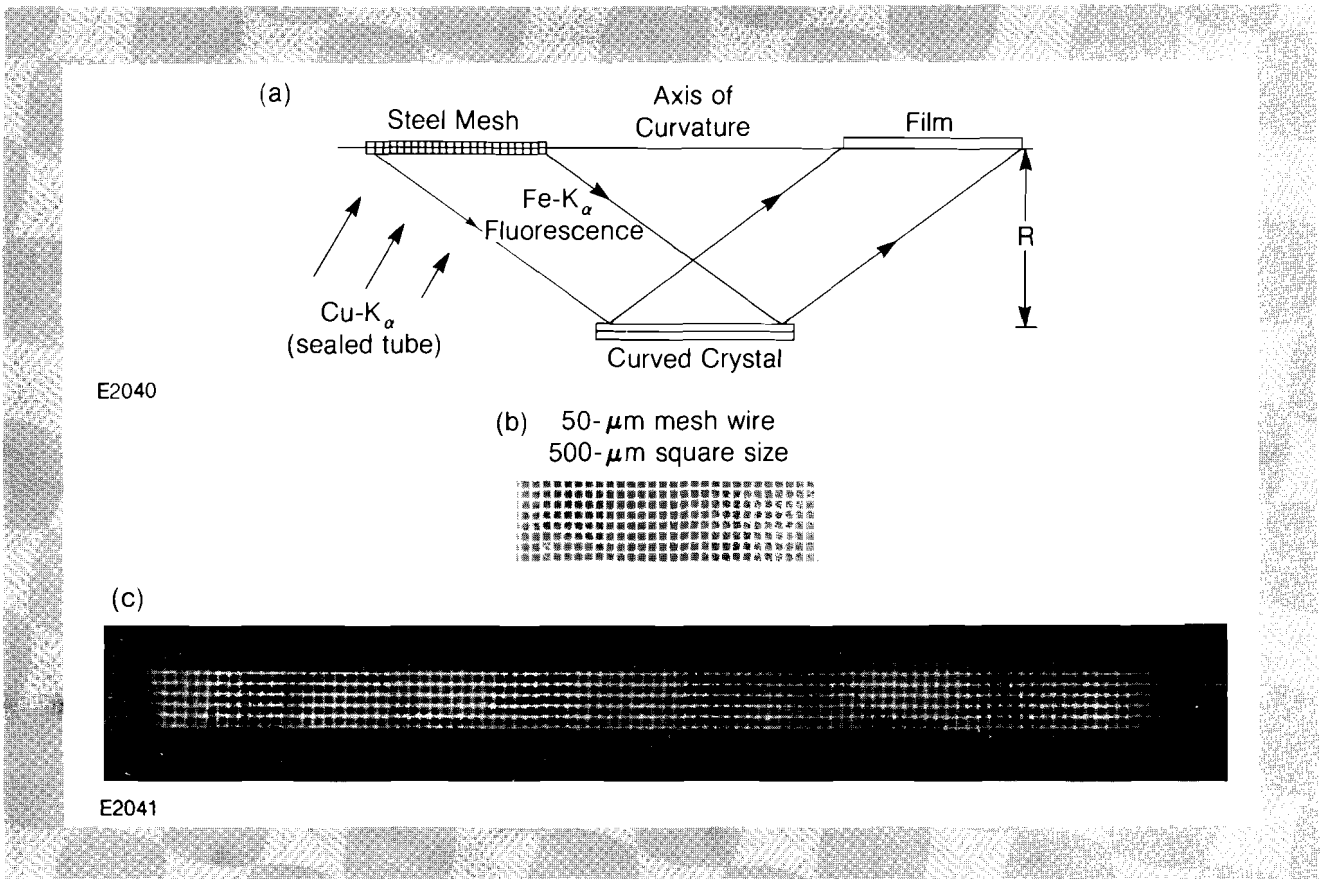

Fig. 11
a): Von-Hamos configuration. The x-ray source (a stainless-steel mesh used to produce Fe K$_\alpha$ radiation) and the film are placed on the axis of curvature of the mica crystal. The flux on the film is considerably enhanced by the curvature of the crystal.

b): Segment of mesh used as test-pattern.

c): Image of test pattern obtained with Von-Hamos spectrometer: imaging in the up-down direction is due to Von-Hamos focusing, and imaging in the left-right (dispersion) direction is due to the mono-chromaticity of the source.
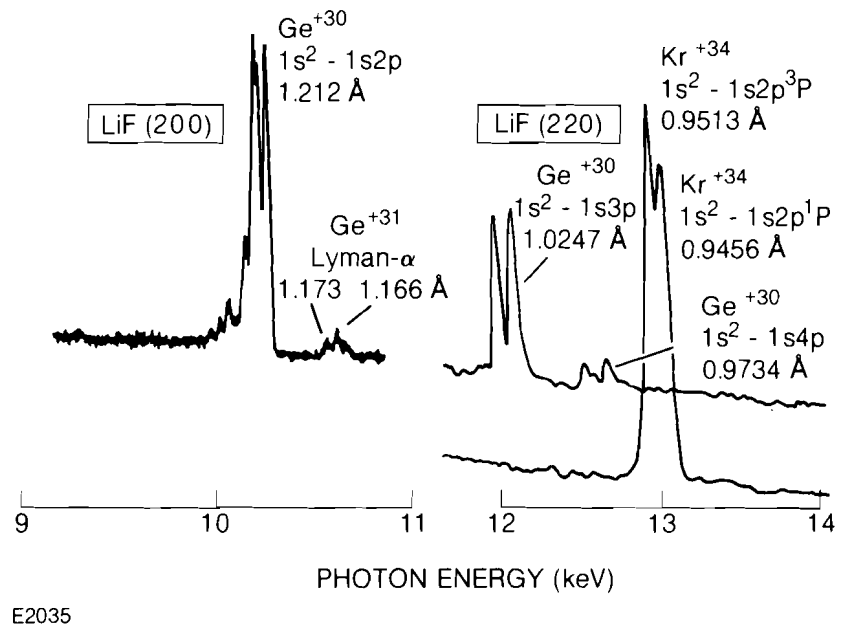
Fig. 12
Spectra obtained by curved LiF (200)
and LiF (220) crystals. Ge lines are from
Germania (GeO₂) shells, Kr lines from
krypton-filled glass shells.

Mosaic Focusing

Mosaic focusing arises from the little-noticed fact that x rays from a monochromatic point source reflected off a mosaic crystal converge to a point of equal distance from the crystal as the source, before diverging away (see Fig. 13). Normally, mosaic crystals are considered to be high-sensitivity, low-resolution diffracting devices. However, recording at the focal position described above, a mosaic crystal simultaneously provides high resolution and sensitivity.

Mosaic focusing is demonstrated by comparing Figs. 14 and 15. In each case the upper spectrum is obtained from a flat pyrolytic-graphite crystal (002), which is highly mosaic with a mosaic spread of about 0.8˝; the lower comparison spectra are recorded by a flat Ge (1 1 1) crystal. The experimental conditions in these two figures are very different; however, the pairs of spectra in each figure correspond to the same laser conditions and the same geometry of the measuring device.

In Fig. 14, the focusing conditions are not met, whereas in Fig. 15 they are. The mosaic focusing is dramatically evident in Fig. 15 where the highly mosaic graphite crystal is shown to have adequate spectral resolution for laser-fusion applications. Moreover, graphite in the focusing geometry retains a higher reflectivity than Ge (1 1 1), by a factor which varies in the range of 10–15 over the spectrum. In fact, to obtain the spectra of Fig. 15, we had to use severe attenuation (~ 4X) to prevent the spectrum produced by the graphite from saturating the film. The fluctuations in the background level are probably due to large-scale crystal inhomogeneities.
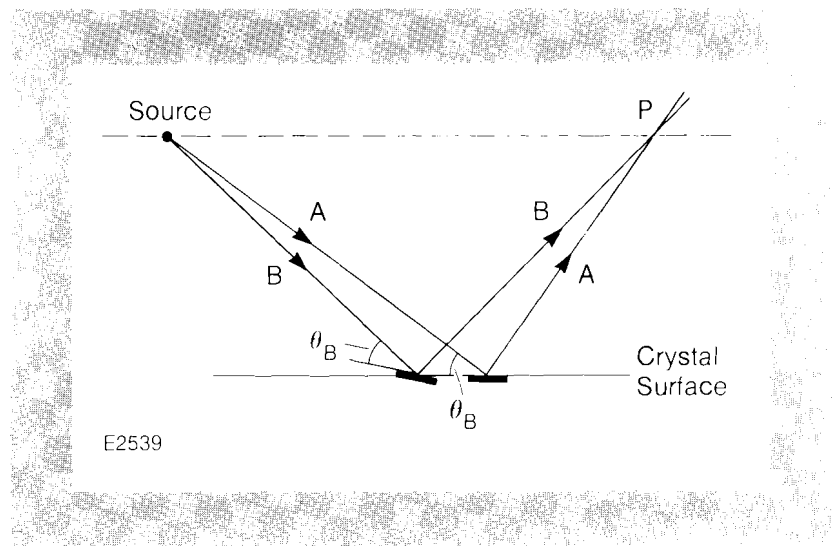
Fig. 13
Focusing from a mosaic crystal. X rays (A) and (B) Bragg-reflect off crystal segments misaligned by small angles from the average crystal plane. Both rays pass through the point P, at which an enhanced x-ray flux will be obtained.
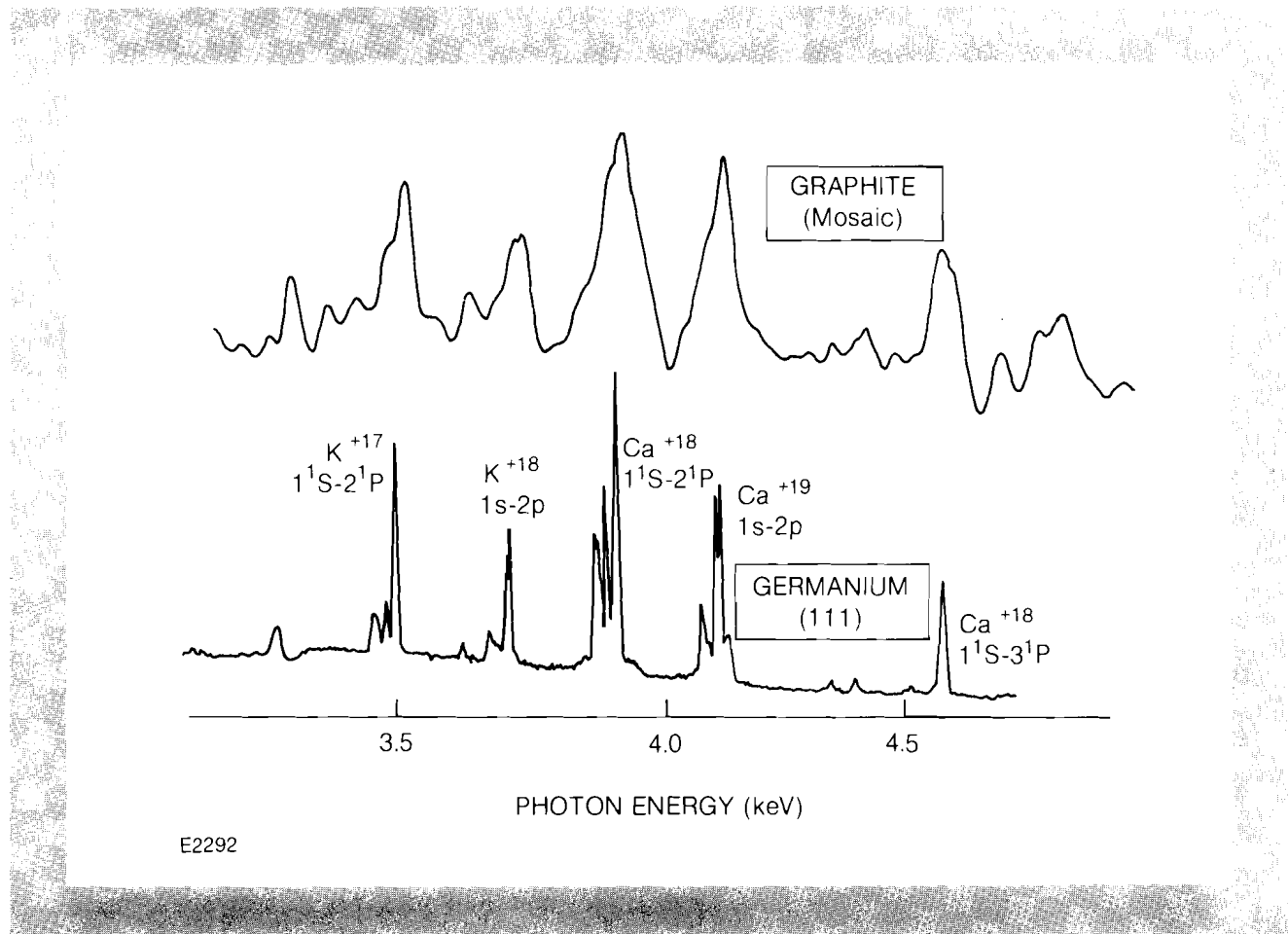

Fig. 14
Effect of mosaic spread in a non-focusing geometry. X-ray spectra from glass impurities are measured simultaneously by a pyrolytic-graphite (002) crystal with 0.8° mosaic spread and a Ge (111) crystal. Laser: ZETA six-beam system, $\lambda = 1.05$ μm, 108 J in 73 ps. Target: glass microballoom, diameter 50 μm, thickness 2.2 μm.
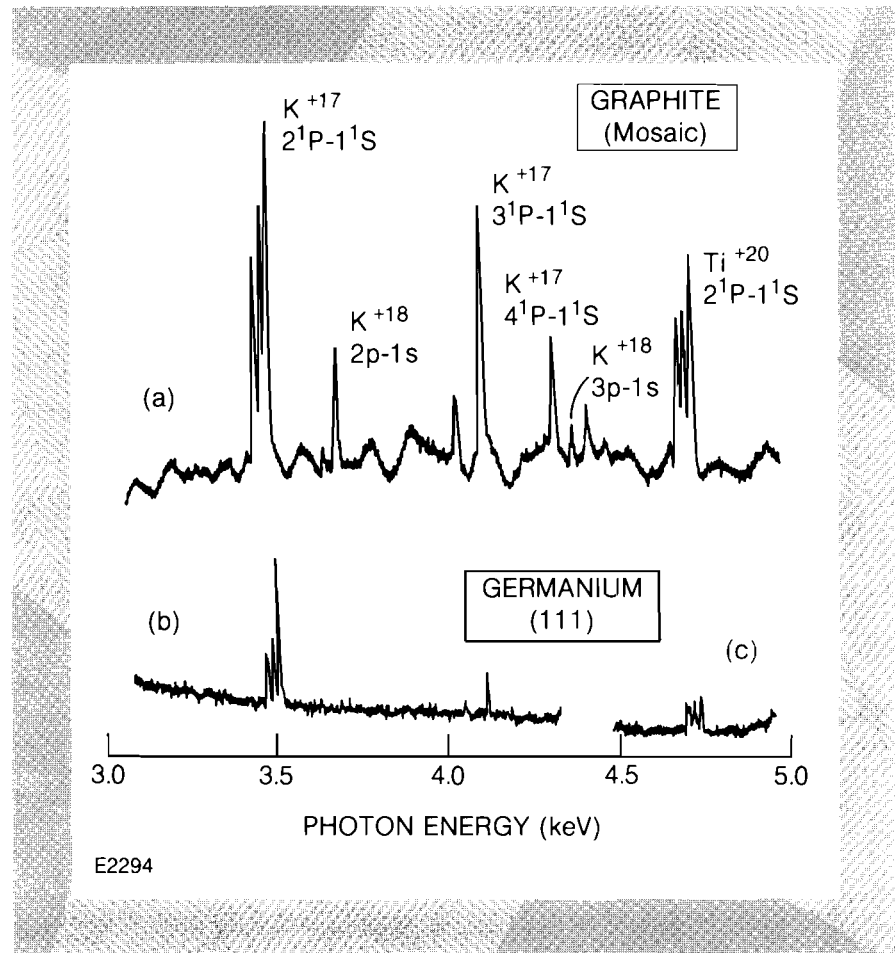

Fig. 15
Demonstration of mosaic focusing.
Graphite (002) and Ge (111) crystals
are both placed in the focusing geometry
of Fig. 13. Spectra in (a) and (b) were
attenuated by a 190-μm-thick mylar foil
to prevent film saturation by the radia-
tion diffracted off the graphite. In (c)
only a 95-μm-thick mylar foil was
employed. The density scale of (b) and
(c) was expanded by a factor of 2 to
make the traces for the two crystals
have more comparable heights.

Achromatic Imaging with Laue Crystal Diffraction

The Laue crystal geometry for x-ray crystal diffraction was described in an earlier issue of the LLE Review.[3] When used in the configuration indicated in Fig. 16, with the film placed at the focus, two-dimensional (achromatic) resolution can be achieved. Imaging in the up-down direction in the plane of the figure is due to the focusing character of Laue diffraction and is of unit magnification. Imaging in the direction perpendicular to the plane of the figure may be obtained either by placing a slit anywhere between the source and the film, or by backlighting the object with a narrow line source. The long dimension of the slit (or the line source) lies in the plane of the figure.

The spatial resolution is limited by the broadening of the beam in traversing the crystal, because of repeated diffraction from successive crystal planes. Clearly it is necessary to etch the crystal down to a small thickness. For thin crystals, the spatial resolution is limited by the angular width of the diffraction rocking curve, which increases when the crystal becomes thinner. For example, for the Ti[+20] resonance line at 2.62 Å, a Ge (111) or Si (111) crystal etched down to a 20-μm thickness can achieve a resolution of about 17 μm. Recent developments in the semi-conductor industry (such as boron implantation) can be used to
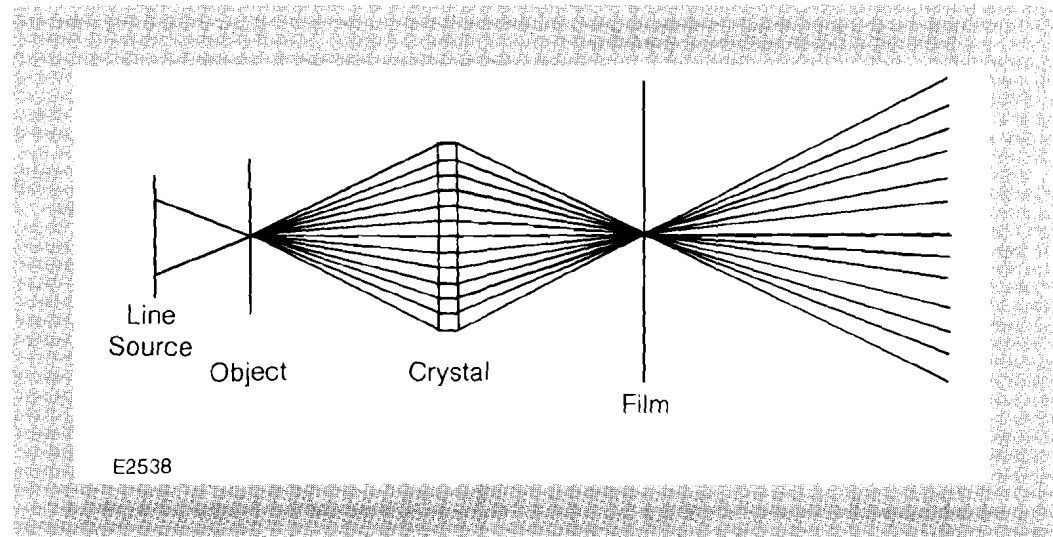
E2538

Fig. 16
Schematic of Laue diffraction geometry. When the film is placed at the focus as indicated, spatial resolution is obtained at the expense of spectral resolution.

fabricate crystals as thin as a few microns. Planar etching can also be used to fabricate such crystals.

In order to demonstrate the two-dimensional imaging capability of the Laue geometry, we used a 3.75-μm-thick Germanium crystal with the (111) Laue diffracting planes. The object was a gold wire mesh, with a fine mesh of 10-μm-thick wire supported on a coarse mesh of 50-μm-thick wire. The mesh and the film were placed at the two conjugate points of the Laue crystal (each 8.4 cm from the crystal) and the mesh was backlit by a Cr x-ray tube ($\lambda = 2.3$ Å). The x-ray tube was positioned so as to project a line focus about 1 cm wide in the direction of dispersion and several microns high. Because of the narrow height of the foreshortened source there was no need for a spatially resolving slit. The image obtained with this setup is shown in Fig. 17, where a resolution of less than 10 μm (in both dimensions) is evident.
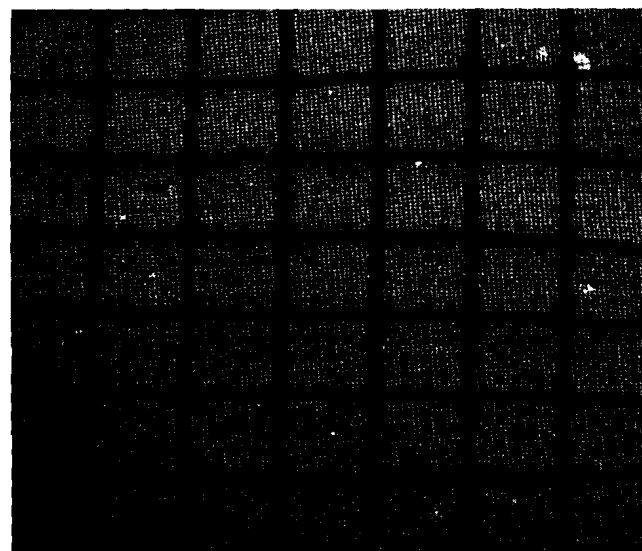
Fig. 17
Two-dimensional achromatic Laue image of a test pattern comprising a 10-μm-thick gold wire mesh placed over a 50-μm-thick wire mesh. Crystal: 3.75-μm-thick Ge (111). Source: Cr x-ray tube (2.3 Å). Dispersion is in the left-right direction.

E2313

$\rightarrow$|$\leftarrow$ 50 μm

This result demonstrates that Laue crystal diffraction can be a useful diagnostic technique for laser-plasma experiments such as backlighting.

REFERENCES
1. B. Yaakobi, R. E. Turner, H. W. Schnopper, and P. O. Taylor, *Rev. Sci. Instrum.* **50,** 1609 (1979).
2. B. Yaakobi and A. J. Burek, LLE Report 139, 1983 (unpublished).
3. LLE Review **11,** 34 (1982).

Section 3
TECHNOLOGICAL DEVELOPMENTS

3.A A Facility for Time-Resolved Low-Angle X-Ray Diffraction Studies
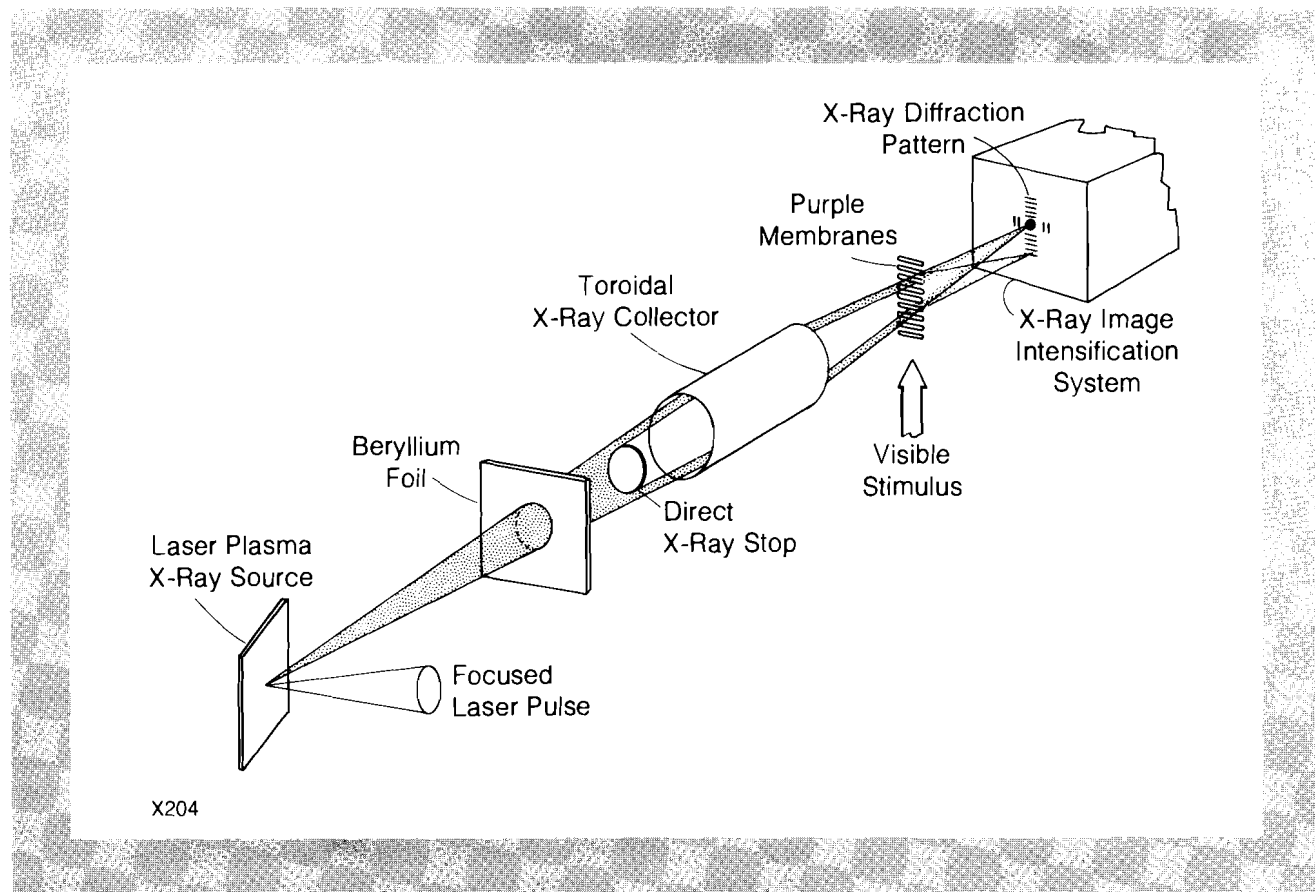
In a previous report[1] we described preliminary results on time-resolved x-ray diffraction from a photostimulated biological system, the purple membrane of the *Halobacterium halobium*. Those results were obtained on a partially completed x-ray-diffraction camera system under development in the GDL experimental facility. In this report, we describe numerous improvements to the facility which permit the single-shot recording of structures having periodic scale lengths between 3 Å and 250 Å. We illustrate this with recent examples of membrane diffraction obtained from various systems. The performance of this laser-driven x-ray-diffraction facility is compared with what is available on other systems, and the prospects for further improvements in performance are summarized.

While the production of intense bursts of x-ray radiation is coincidental in direct-drive inertial-fusion target experiments, laser-produced plasmas may also be employed for the express purpose of generating intense x rays. For laser-heating pulses of a nanosecond or less, the hot, high-density plasma formed near the surface of a solid target by a single, focused laser pulse has several important characteristics as an x-ray emitter. The dimensions of the x-ray-emitting region are small, with the lateral extent comparable to the size of the laser focal spot. The x-ray emission, especially for photon energies above one kilovolt, closely follows the laser-pulse time history. Depending on the choice of target,

intense monochromatic line radiation may be produced at many wavelengths between 1.5 Å and 5 Å. Recently, the greatly improved plasma heating characteristics of the frequency-tripled Nd: glass laser radiation from GDL has enabled us to produce such monochromatic line radiation near 3 keV with a conversion efficiency (of laser energy into x rays) of 1 to 2%.[2]

Since the x-ray source is driven by a laser, it may readily be synchronized with a wide variety of external events and thus serve to create a probe beam for the study of kinetic structural phenomena down to atomic-scale resolution. Because the x-ray emission is, roughly speaking, isotropic, the design of a suitable x-ray probe-beam facility presents a challenge in maximizing the collection and transport of x rays. In our application, namely low-angle x-ray diffraction, the net divergence of the beam translates directly into the angular resolution of the system, so our x-ray optical system was constrained to be a focusing system. The point nature of the laser-driven source is very important in that it permits a simple, high-efficiency focusing system to be constructed at grazing angles of reflection. Our design is shown schematically in Fig. 18. We use a toroidal mirror in the form of a truncated ellipsoid to focus the x rays.[3] In this geometry it can be shown that the maximum useful collection solid angle is of the order of θ_c^2, where θ_c is the critical angle for total reflection of x rays. The critical angle depends upon the material properties of the mirror surface as well as the

Fig. 18
Conceptual layout of pulsed x-ray-diffraction experiment.

x-ray wavelength. Nickel is a good choice for reflection of x rays in the 2- to 5-Å range and results in a collection solid angle of approximately 2×10^{-4} sr for such a system. Our mirror was fabricated from a CERVIT™ substrate in the optical shop at the University of Rochester and coated with nickel in the LLE target-fabrication facility. It has a focal length of 86 cm.

The specular beam reflected from this mirror has an annular structure which must be taken into account in preparing and aligning specimens in the camera. A space of approximately 20 cm is available in front of focus to position specimens. This space is isolated from the rest of the laser-plasma target chambers by a vacuum window, allowing the specimen environment (temperature, atmosphere, humidity, etc.) to be controlled by the experimenter. On the vacuum side of the window, a narrow annular stop absorbs most of the non-specular x rays scattered from the finite micro-structure of the mirror surface. In recent x-ray diffraction experiments, 10^{10} photons of foil-filtered monochromatic x rays at 4.45Å were routinely delivered to specimens on each GDL laser shot.

It is interesting to compare the performance of this low-angle, beamline facility with both conventional laboratory facilities and synchronous electron-storage-ring facilities. In Fig. 19 we plot
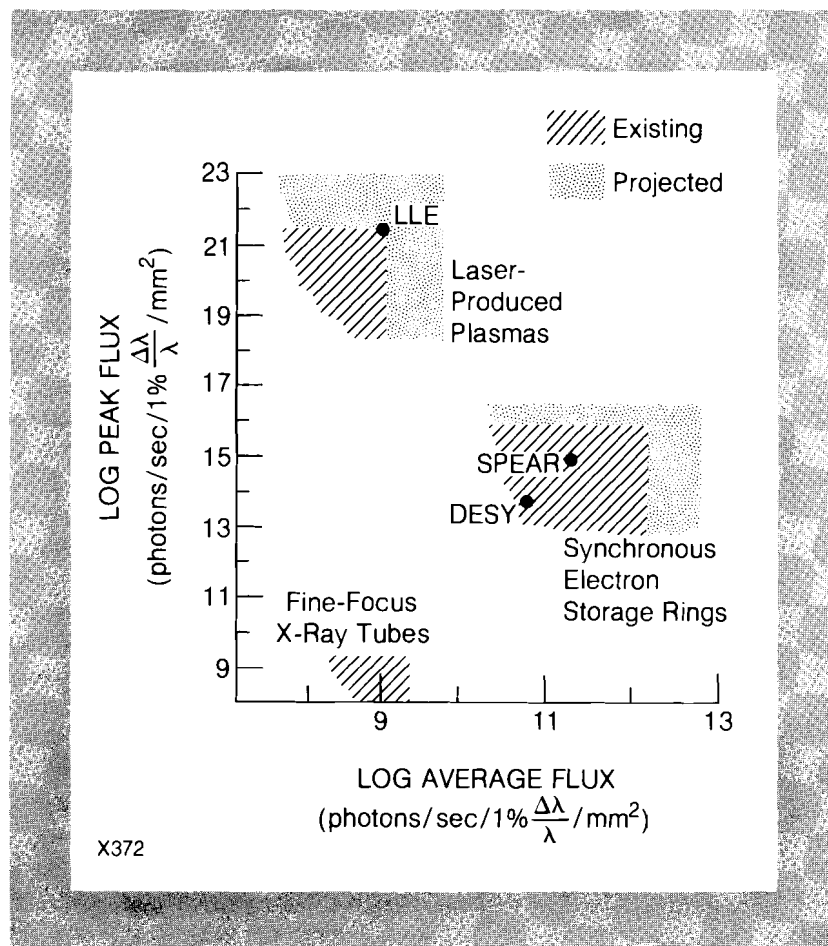

Fig. 19
Peak versus average flux delivery of typical x-ray sources in low-angle diffraction experiments.

the peak and average flux delivery capabilities of these systems. It is clear that the GDL facility can generate diffraction data at a rate equal to the best laboratory facilities while doing so with a potential time resolution many orders of magnitude faster than storage-ring facilities. In order to realize this level of performance, however, great care must be given to the design of the detection system in laser-plasma experiments. Because of the unprecedented delivery rate of x rays in this case, it is impossible to use counter tubes of any currently available design as detectors. Solid-state detectors have many desirable characteristics but are not yet available in sufficiently large-area arrays to be suitable for this application. On the other hand, because of the windows used, TV detectors have no soft-x-ray response. This latter problem is overcome by using a thin scintillator material to convert the x rays to visible light. Although this latter idea is simple in principle, its satisfactory implementation into our system proved very difficult until recently, because of a subtle property of the high numerical aperture of the x-ray focusing optics: the true focal surface of the camera is a sphere tangent to the focus of the camera and to the specimen. The effects of this curvature are not noticed in long-focal-length or low-numerical-aperture systems because they exhibit a large depth of focus. However, in our preliminary experiments on diffraction from purple membrane[1] we were limited to observation at low scattering angles, in part because of serious defocusing near the edges of our flat scintillator plate. Even with a 40-mm-diameter detection field, observation of the highest-angle diffracted orders from purple membrane required a specimen position only 3.5 cm from focus.

Uniform deposition of a thin scintillator onto steeply curved surfaces by commercial vendors has proved to be difficult. It appeared that we could acquire data of satisfactory quality with a focal sphere 5 cm in diameter, and success in such a scintillator deposition was achieved by Thomas Electronics, Inc. In our present camera, the scintillator is deposited on a special fiberoptic plate in which the individual fiber axes are at near-normal incidence to the curved scintillator surface as well as to the flat output surface.

Photons from the scintillator are coupled directly to a VARO 40-mm microchannelplate (MCP) image intensifier set to a gain of 40,000. The MCP output is then lens-coupled to a commercial, refrigerated, digital TV detector (Princeton Applied Research OMA II) operated in a fully two-dimensional mode by means of an LSI 11/23 computer system. The TV detector is operated at $-25°C$ with multiple, high-voltage, slow-scan readout of the image for maximum sensitivity and linear dynamic range.

The performance which may be obtained from our x-ray-diffraction camera is shown in Fig. 20. This is a powder diffraction pattern obtained from a dried pellet of purple membrane with a single shot of 45 J at 0.351 μm from GDL. A sector of the diffraction pattern was circularly averaged in the LSI 11/23 computer to
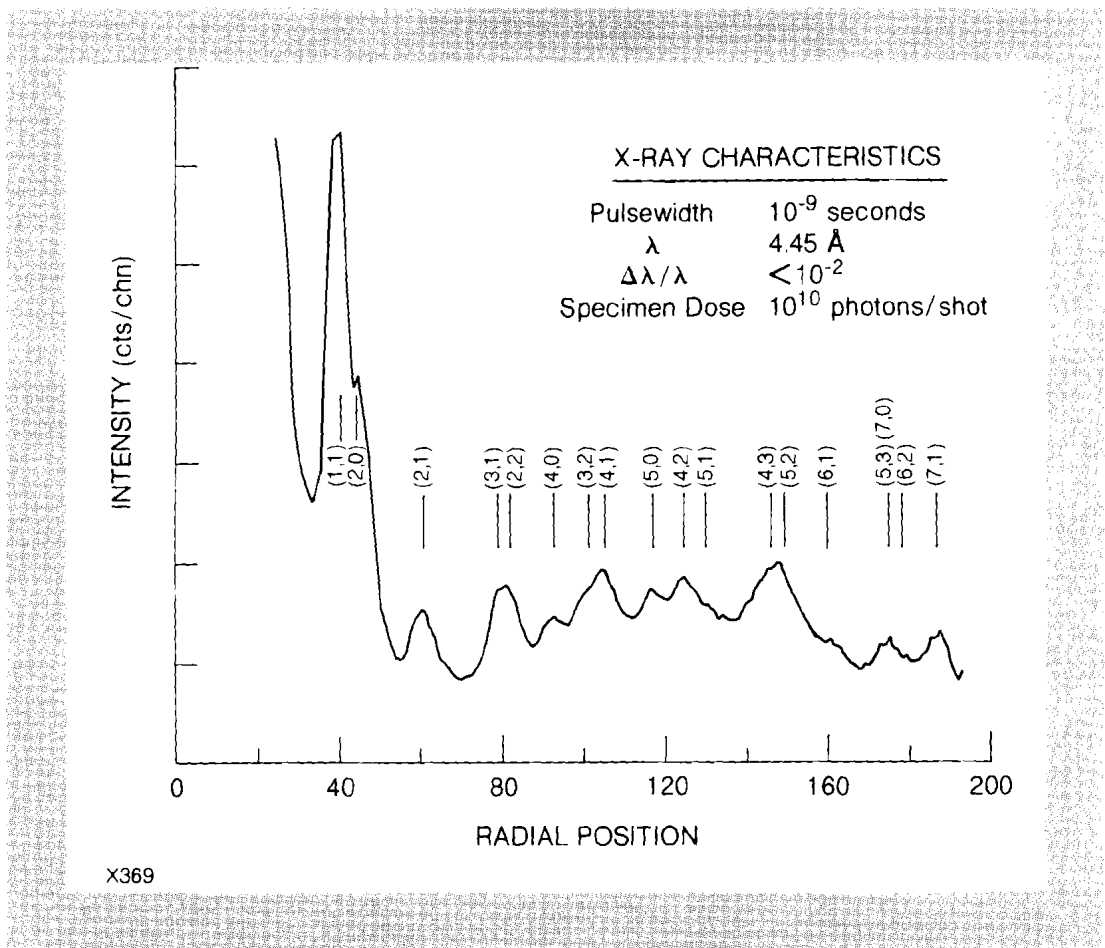
Fig. 20
Azimuthally averaged powder x-ray diffraction pattern from a dried pellet of purple membrane from "Halobacterium halobium." Peaks are shown indexed on a hexagonal, two-dimensional lattice out to 7-Å resolution. A single shot from the frequency-tripled GDL facility was used to acquire this pattern.

produce this display. The specimen consists of an array of membrane fragments which are primarily two-dimensional in crystalline character. The reflections are indexed on a two-dimensional hexagonal lattice after Henderson.[4] The highest-order reflection shown corresponds to 7-Å resolution in the plane of the membrane (and is the highest-order reflection to be reliably phased by any group to date). Experiments to observe structural changes in purple membrane on photostimulation, begun some time ago, have greatly benefited from this improved performance. Significant alterations in the relative intensities of many of the high-order reflections are observed 1 ms after photostimulation of the specimens while little change is noted 200 μs after photostimulation.[5] This timescale corresponds to the time in the purple-membrane photocycle when hydrogen-ion release occurs. The results of further experimentation and analysis on the purple membrane will be presented in a future report.

Other membrane ion-transport experiments are also being conducted, in collaboration with NLUF participants. To date these experiments have concentrated on studies of sample preparation, and handling problems associated with the unique configuration of our camera. A preliminary experiment performed during the quarter recorded a diffraction pattern from a layered

preparation of sarcoplasmic reticulum prepared by J. Kent Blaise and Donnatella Pascolline (University of Pennsylvania). Future reports will give further details of these experiments. For the present report, we note that this specimen is characterized by a rather large basic structural period of the order of 200 Å or so, depending on the relative humidity. A display of a single-shot diffraction pattern recorded on our TV detector from this specimen is given in Fig. 21. Our ability to observe the first-order peak in the diffraction pattern is significant in that kinetic studies of relatively long-period samples such as polymer systems would appear quite feasible with this apparatus.

Zero Order →

First Order (220 Å) →

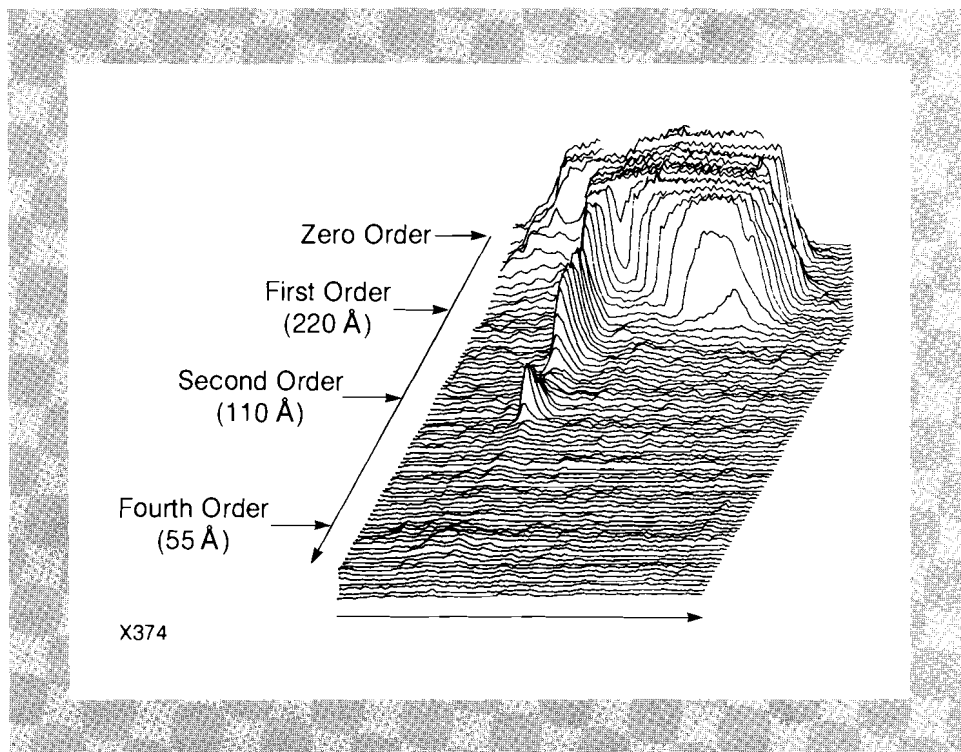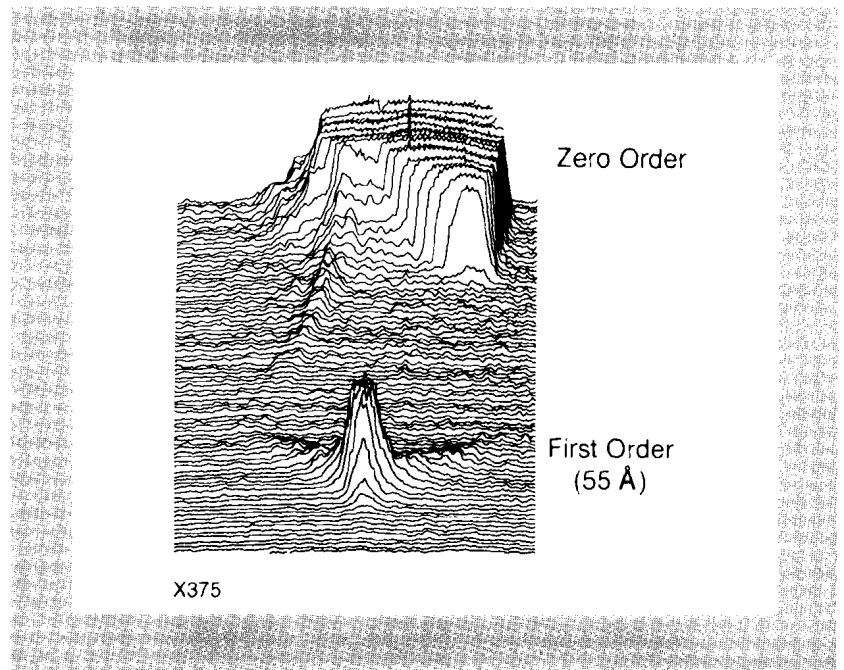Second Order (110 Å) →

Fourth Order (55 Å) →

X374

Fig. 21
Two-dimensional display of a single-shot x-ray diffraction pattern from sarcoplasmic reticulum. The first-order peak corresponds to a period of 220 Å.

Single-shot diffraction from a synthetic multilayer, composed of dipalmitoyl lecithin, is shown in Fig. 22. Although the peak of the first-order (55-Å) scattering has saturated the detector, the disorder in the multilayer (mosaic spread) is evident from the arc-like scattering around the peak. The lecithin compound was also prepared by the University of Pennsylvania group as a calibration compound for the sarcoplasmic-reticulum experiment. This pattern also shows the low-angle capabilities of the facility.

The biological systems studied to date, although relatively weak x-ray scatters, are nevertheless ordered systems. It is of interest to some workers to study structural kinetics in poorly ordered systems such as solutions. Many chemical or biochemical reactions such as enzyme-substrate interactions, protein folding, etc. could be studied in detail if the available x-ray fluxes could be increased. In fact, we anticipate such a flux increase in our system toward the end of 1983 with the completion of the active-mirror upgrade and a larger-aperture frequency conversion of the GDL

Fig. 22
Two-dimensional display of a single-shot x-ray diffraction pattern from dipalmitoyl lecithin. The first-order peak has saturated the TV detector but the intense signal level permits direct observation of the mosaic spread in the sample from the arc-like scattering surrounding the peak.

facility. When combined with expected improvements in x-ray yields from highly chlorinated target materials, we expect to deliver up to 10^{11} x-ray photons per shot to specimens in our camera.

Summary

The past two decades have seen extensive development of high-average-power x-ray sources with great improvements in conventional structural measurements, such as crystallography, and the introduction of entirely new techniques, such as extended x-ray-absorption fine structure (EXAFS). The introduction of the laser-driven x-ray source as a structural analytic tool will have an impact on a broad range of scientific and technological problems by greatly extending our capabilities for time-resolved measurements of bulk structures.

REFERENCES

1. LLE Review **8**, 17 (1981).

2. B. Yaakobi, P. Bourke, Y. Conturie, J. Delettrez, J. M. Forsyth, R. D. Frankel, L. M. Goldman, R. L. McCrory, W. Seka, and J. M. Soures, *Opt. Commun.* **38**, 196 (1981).

3. B. L. Henke and J. W. M. DuMond, *J. Appl. Phys.* **26**, 903 (1955).

4. R. Henderson, *J. Mol. Biol.* **93**, 123 (1975).

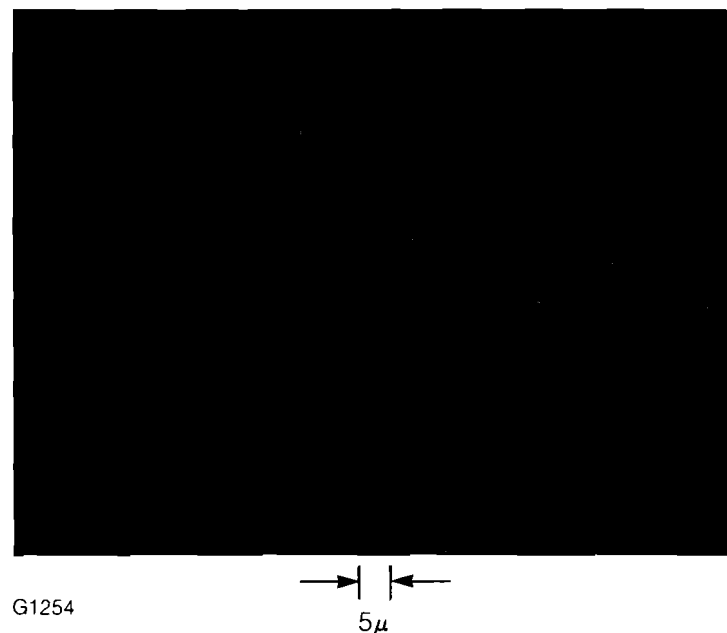5. R. D. Frankel and J. M. Forsyth, *Biophys. Journal* **41**, 15a (1983).

3.B   Defects and Damage in Thin Films

As the laser-fusion community proceeds to frequency-convert Nd:glass laser systems to shorter wavelengths, the importance of the performance of optical coatings at these wavelengths becomes of greater interest. Of particular interest to the LLE program is the performance of these coatings at the tripled frequency of Nd:glass, 351 nm. The fluence level at which the optical coatings can transport the UV beam will have a major impact on the size, cost, and energy-on-target of all UV upgrades to the OMEGA laser. We have therefore developed an experimental system to characterize better the damage process in thin-film coatings.

Presently the most successful theory[1,2] describing the damage of optical thin films by high-power laser radiation attributes the damage process to isolated microscopic impurities, or defects, in the deposited coating. According to this theory, the impurity absorbs the incident radiation causing its temperature to rise, eventually producing melting, vaporization, or fracture of the material surrounding the impurity.

This impurity model can explain many of the scaling effects observed in thin-film damage studies. The observed decrease in damage threshold with decreasing wavelength can be attributed to the increase in Mie absorption with decreasing particle size, and the well-known result that Mie scattering is strongest for particles whose size is comparable to the incident light wavelength. The observation that the damage threshold increases with thinner films can be explained by the exclusion of larger, easier-to-damage, impurities as the physical thickness of the film is reduced. The observation of very high damage thresholds for small incident-laser spot sizes is consistent with damage being caused by localized impurities: when the spot size is small

Fig. 23
Photomicrograph of typical damage to a Ta_2O_5-SiO_2 high-reflectance (HR) coating. Note in particular the micron-sized pits.
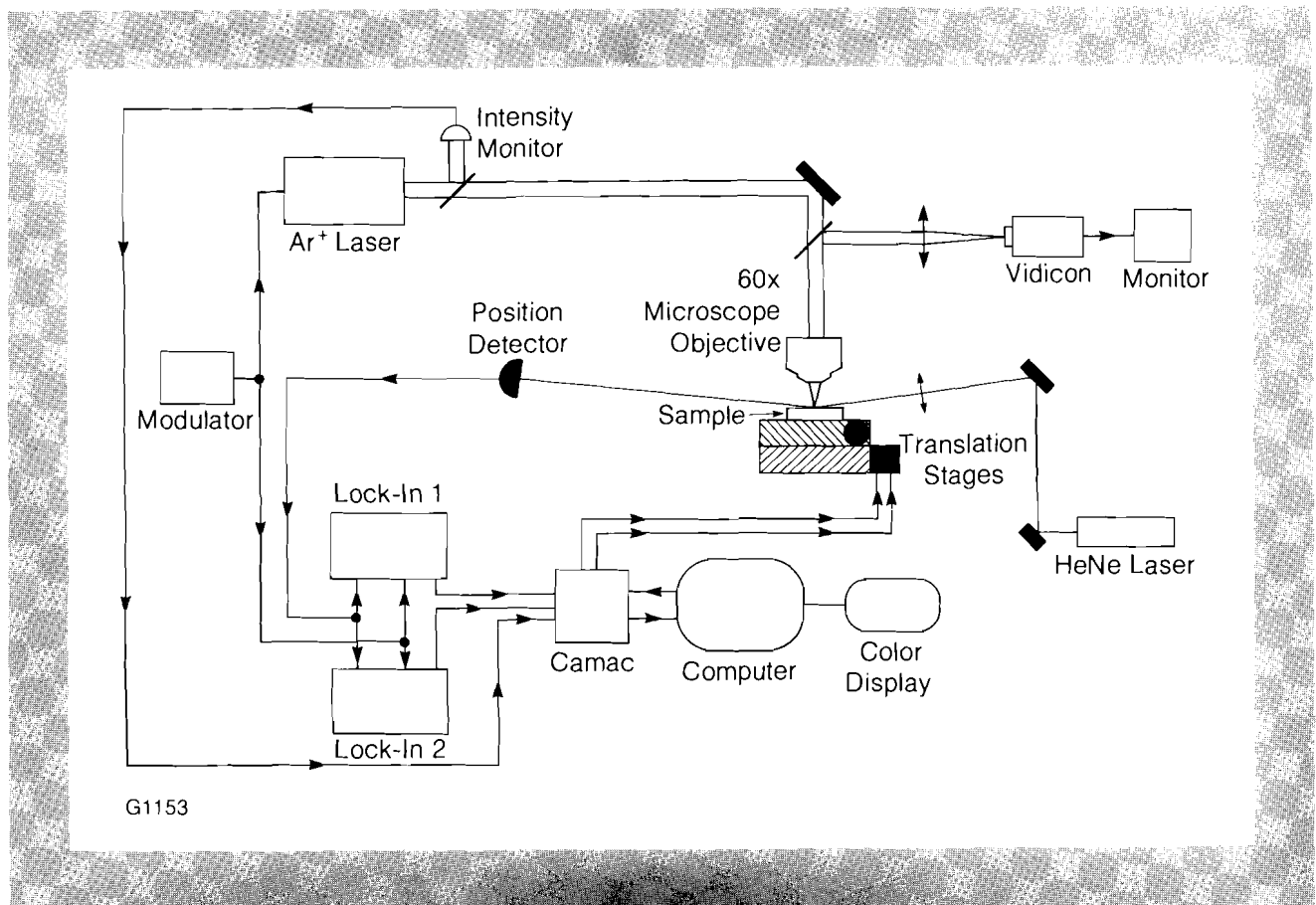
G1254

5μ

compared with the mean distance between impurities, it is possible to avoid these weaker areas and measure higher thresholds. In addition, it has been shown for oxide and fluoride films that the dependence of damage and thermal properties on laser pulse width is consistent with the impurity model.[1]

Very little, however, is known about the exact nature or density of these damage-causing impurities. It has been determined from damage morphology[3-5] that the impurities must be small in size, typically several microns or less in diameter. Figure 23 shows a photomicrograph of the typical morphology seen as a result of laser-induced damage. In this work we have set out to establish a direct connection between the localized absorption properties of a thin film and the appearance of damage in areas of locally high absorption.

Detection of Impurities

Several attempts have been made to use photothermal effects to investigate surface and subsurface structure in solids and in thin films.[6-11] Photothermal imaging has developed into a very powerful non-destructive testing technique. All previous methods have lacked sufficient spatial resolution to detect the objects of interest to laser-damage studies, of size ≤ 1 μm. Some defects have been seen in thin films,[7-10] but their size, typically 20 microns

Fig. 24
Block diagram of the "Mirage" apparatus for photothermal deflection.
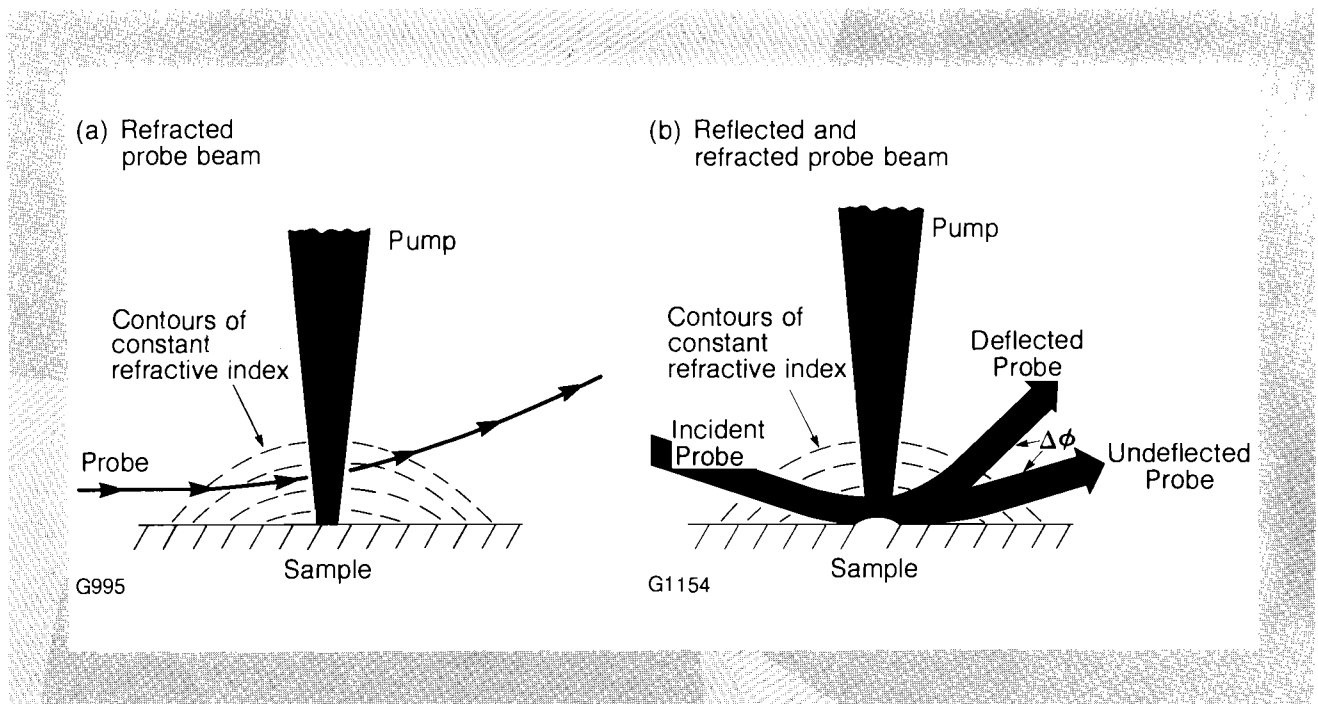

G1153

or larger, is not consistent with the experimental observation of micron-size pits in damage coatings at threshold (see Fig. 23).

The apparatus we have used to locate micron-size absorbing impurities in dielectric thin films is shown schematically in Fig. 24. It relies on the photothermal deflection[11] of a probe laser to measure the absorption, in a localized area, of energy from the pump laser. The pump beam consists of modulated 0.351-μm light from an argon-ion laser focused to a 1.0 ± 0.2-μm-diameter spot by a 60X microscope objective. The sample of interest is kinematically mounted on a computer-controlled X-Y translation stage, with a minimum step size of 0.4 μm. A HeNe laser probe beam has been used in two geometries: skimming across the sample (Fig. 25a), and reflecting off the sample surface at a shallow angle (Fig. 25b).[10] The probe beam is focused to a spot size of 75 μm in the vicinity of the pump-beam focus. The two probe-beam geometries have been compared and the second (reflective) method has shown a sensitivity greater by a factor of ten. This can most probably be attributed to a new photothermal effect first discussed by Olmstead et al.[12]

In the skimming geometry (Fig. 25a), the probe beam is deflected by a refractive-index gradient, caused by the temperature gradient set up when the pump beam is absorbed locally by an impurity in the sample. This effect is also present in the reflective geometry (Fig. 25b), but here the probe beam is also deflected off the "bump" caused by the local heating and resulting thermal expansion of the substrate. The modulated position of the probe laser is measured by a position sensor (United Detector Technologies SC-25) connected to a set of lock-in amplifiers arranged in quadrature to measure both the amplitude and phase
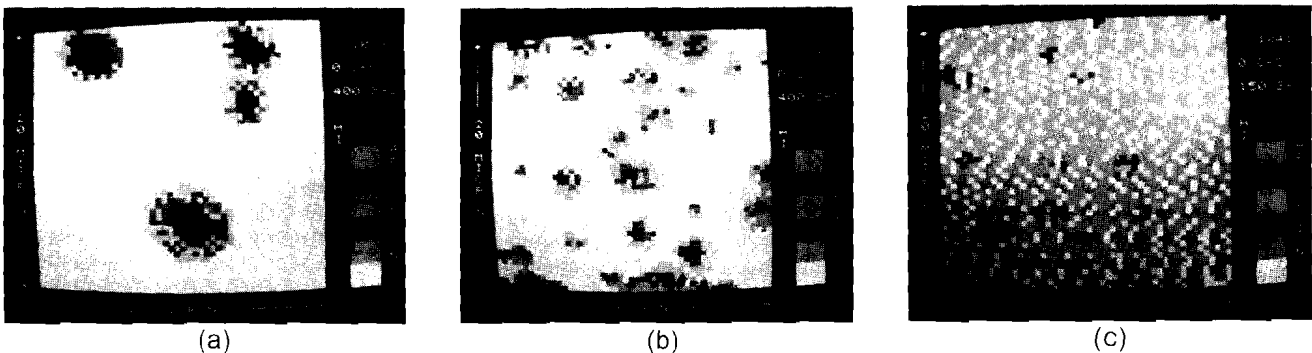
Fig. 25
Use of the "Mirage" effect for mapping defects in a thin-film sample. Pump-laser energy is absorbed by a defect with two consequences: (1) the surrounding air is heated, leading to a refractive-index gradient; and (2) thermal expansion in the absorption region causes a "bump" to form on the sample surface. Depending on the geometry chosen, the probe laser is either refracted [case (a)] or reflected as well as refracted [case (b)].

(a) Refracted probe beam

Pump

Contours of constant refractive index

Probe

G995   Sample

(b) Reflected and refracted probe beam

Pump

Contours of constant refractive index

Deflected Probe

Incident Probe

Δφ Undeflected Probe

G1154   Sample

of the position signal. A DEC-11/23 computer controls the position of the sample and reads the output of the lock-in amplifiers. False-color absorption maps of the coatings being studied are produced on a Chromatics color-graphics display. The spatial resolution obtainable using this technique is illustrated in Fig. 26, where scans of absorbing sites of Cr spots of various diameters ($\leq 5\ \mu m$, $\leq 1\ \mu m$, and $\leq 0.4\ \mu m$) are shown. The 0.4-μm sites are clearly resolvable.

When the cross section of the absorbing volume becomes smaller than the diameter of the pump beam, only a portion of the incident energy is transformed into heat and into the resulting thermal and acoustic waves. The ultimate detectivity in this case will depend not only on the absorption coefficient and the thickness of the inclusion, but also on the ratio of the cross sections of the pump beam and the absorbing region, the distance between the inclusion and the coating-substrate interface, and the thermal properties of the material in which the inclusion is embedded. It should be clear that the pump-beam spot size must be kept as small as possible in order to detect the absorbing inclusions in thin films with maximum sensitivity.

(a)   (b)   (c)

G1253

Fig. 26
Absorption maps of Cr impurity particles of various diameters (d).
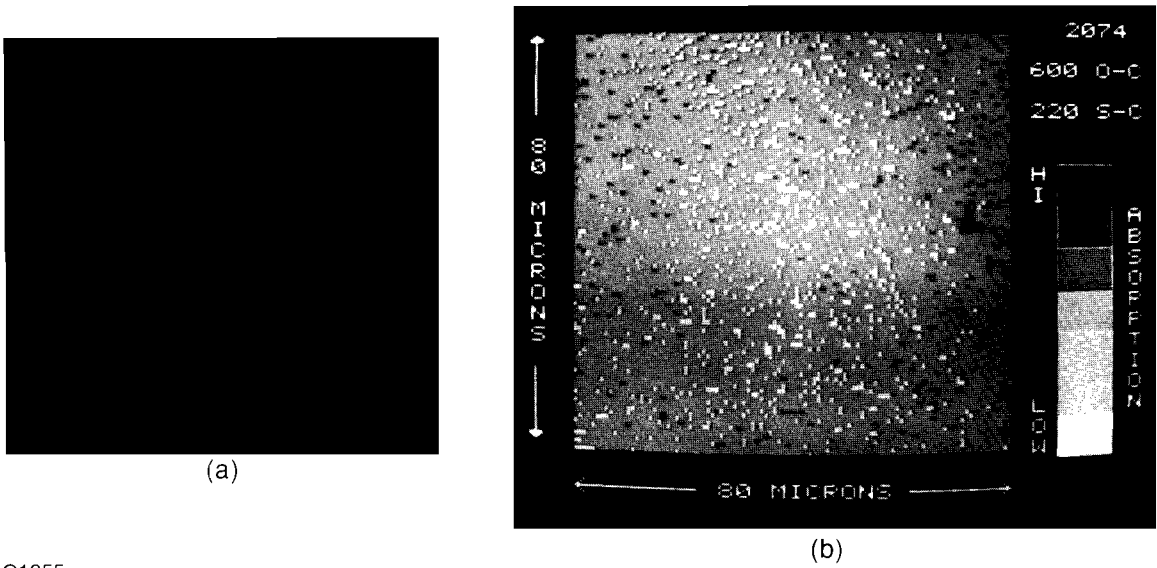*(a) d ≤ 5 μm*
(b) d ≤ 1 μm
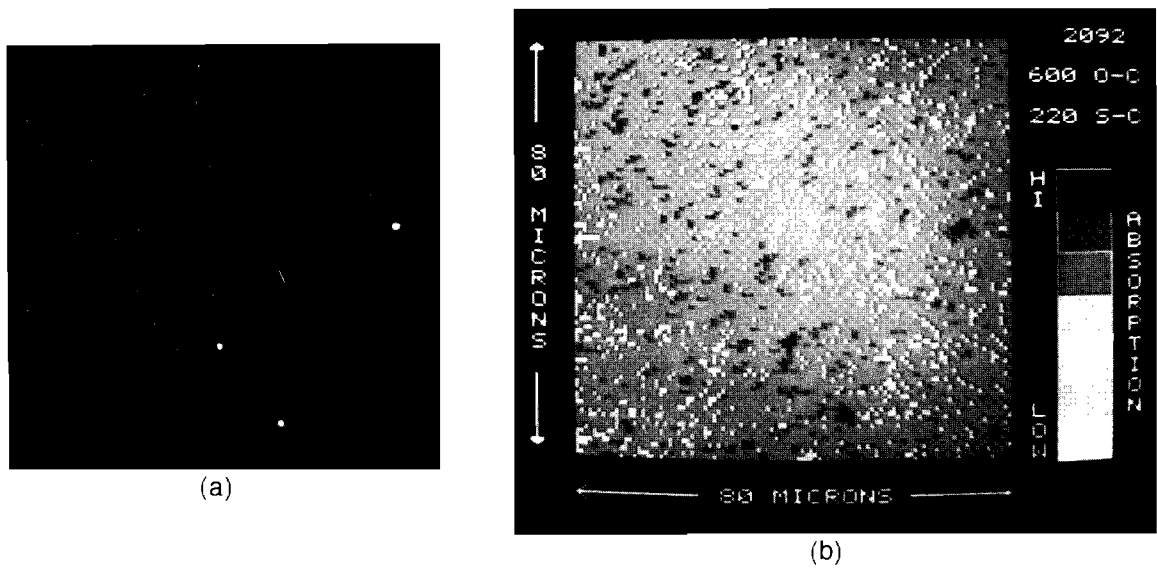*(c) d ≤ 0.4 μm*

Impurities and Damage

In order to demonstrate a connection between absorptive impurities and damage, we have made absorption maps of several coatings and then exposed them to high-intensity laser light on the LLE UV damage-testing facility.[13] Photomicrographs and absorption maps of sample coatings were taken both before and after the damage test. Typical examples are shown in Figs. 27 and 28. In many cases the absorption map before damage shows small areas of high absorption that are not visible in the dark-field photomicrographs (see Fig. 27). When the coating shown in Fig. 27 was exposed to a laser irradiance approximately 20% above its damage threshold, three localized areas on the coating were damaged as is seen in the photomicrograph of Fig. 28a.

In addition, the absorption map of the same area (Fig. 28b) shows clearly increased absorption in the region which showed a defect in Fig. 27b. There are also two areas which show damage in Fig. 28b but no strong absorption signature in Fig. 27b. In these cases, it is uncertain whether our sensitivity is insufficient to

(a)

(b)

G1255

Fig. 27
(a) Photomicrograph and (b) absorption
map of Ta_2O_5-SiO_2 HR coating before
damage test.

(a)

(b)

G1256

Fig. 28
(a) Photomicrograph and (b) absorption
map of Ta_2O_5-SiO_2 HR coating after
damage test.

detect the damage-causing impurities, or whether other mech-
anisms besides linear absorption are acting to initiate some of the
damage. Attempts are being made to increase the sensitivity of
our apparatus in order to explore this question further.

Conclusion

We have taken a first step toward understanding the role of absorptive inclusions in the damage process of thin films. We have demonstrated that photothermal-deflection microscopy can detect submicron absorbing impurities in optical coatings. In the future, we plan to identify the exact nature of these damage-causing impurities. It is hoped that optical coatings of increased damage resistance will be obtained by the use of measures to control these impurities in the manufacturing process.

REFERENCES

1. T. W. Walker, A. H. Guenther, and P. E. Nielsen, *IEEE J. Quantum Electron.* **17,** 2053 (1981).

2. See references 21-48 in Ref. 1.

3. W. H. Lowdermilk, D. Milam, and F. Rainer, in *"Laser-Induced Damage in Optical Materials,"* edited by H. E. Bennett, A. J. Glass, A. H. Guenther, and B. E. Newnam, NBS Special Publ. 568, 391, Washington, D.C., GPO (1979).

4. C. K. Carniglia, J. H. Apfel, T. H. Allen, T. A. Tyttle, W. H. Lowdermilk, D. Milam, and F. Rainer, in *"Laser-Induced Damage in Optical Materials,"* edited by H. E. Bennett, A. J. Glass, A. H. Guenther, and B. E. Newnam, NBS Special Publ. 568, 377, Washington, D.C., GPO (1979).

5. T. W. Walker, A. H. Guenther, and P. E. Nielsen, *IEEE J. Quantum Electron.* **17,** 2041 (1981).

6. Y. H. Wong, R. L. Thomas, and G. F. Hawkins, *Appl. Phys. Lett.* **32,** 538 (1978).

7. R. P. Freese and K. J. Teegarden, in *"Laser-Induced Damage in Optical Materials,"* edited by H. E. Bennett, A. J. Glass, A. H. Guenther, and B. E. Newnam, NBS Special Publ. 568, 313, Washington, D.C., GPO (1979).

8. D. S. Atlas, M. S. Thesis, Institute of Optics, University of Rochester, 1981.

9. J. A. Abate, S. D. Jacobs, W. S. Piskorowski, and T. P. Pottenger, *Proceedings of the Second Conference on Lasers and Electro-Optics (CLEO),* Phoenix, AZ (1982).

10. W. C. Mundy, R. S. Hughes, and C. K. Carniglia in *"Laser-Induced Damage in Optical Materials,"* edited by H. F. Bennett, A. H. Guenther, D. Milam, and B. Newnam, NBS Special Publication, 1982 (to be published).

11. A. C. Boccara, D. Fournier, and J. Badoz, *Appl. Phys. Lett.* **36,** 130 (1980).

12. M. Olmstead, N. M. Amer, D. Fournier, and A. C. Boccara, *Appl. Phys.* (to be published).

13. J. A. Abate, R. Roides, S. D. Jacobs, W. Piskorowski, and T. Chipp in "Laser-Induced Damage in Optical Materials," NBS Special Publication, 1982 (to be published).

3.C Development of Metal-Doped Polymer Ablation Materials

Some inertial-fusion target designs specify ablator coatings with a high average atomic number (Z), in order to minimize the fusion-fuel preheat caused by superthermal electrons or radiation originating in the target corona.[1] Low-Z materials with up to several atomic percent of a high-Z element uniformly dispersed on an atomic scale are desirable in this type of target.

We have investigated two polymeric materials for incorporating high-Z metallic elements into ablation layers. Although each method utilizes solution-coating techniques, the materials and the resulting structures are basically different. The first, sulfonated polystyrene, which has a metal content of up to 5 atomic percent, is easily prepared and can easily be coated from solution. The second material is a styrene-butadiene copolymer in which stable iron colloids are dispersed. In sulfonated polystyrene the metal atoms are expected to be homogeneously dispersed in the polystyrene matrix on the molecular scale. In the metal-colloid-seeded polymer the metal dispersion is less uniform, but a broader range of average Z is possible.

We have also investigated two methods for coating the polymer solutions onto glass-microballoon targets. One technique involves dipping a stalk-mounted target into the solution; the other uses an acoustic-levitation device,[2,3] wherein the target is placed into an acoustic potential well. The solution-dipping technique has the advantage of simplicity, but is limited by the difficulty of obtaining uniform coatings thicker than 0.5 μm. Using the acoustic-levitation approach special care must be taken to ensure concentricity of the coating and the target, but thicker coatings are achievable.

Metal-Loaded Polymeric Materials

The first material, fully sulfonated polystyrene, is easily soluble in water. The acid form, in 30% aqueous solution with an average molecular weight of 120,000 and a high degree of substitution (90 to 100%), was obtained from the National Starch and Chemical Company.[4] It was neutralized with hydroxides of various alkali and alkaline-earth metals.

The polymer contains five atomic percent metal if neutralized with alkali metals, and 2.5 atomic percent if neutralized with alkaline earth metals. Average Z's range from 4.8 to 7.5, the largest value occurring with Cs neutralization. This is in contrast with Z=2.7 for polyethylene and Z=3.5 for parylene. Full neutralization of sulfonated polystyrene was performed by adding a stoichiometric amount of a metal hydroxide. The reaction proceeded rapidly at room temperature. The viscosity of the 30% aqueous sulfonated polystyrene was 150 cps. For our experiments, the viscosity was increased to 300 cps by freeze-drying and redissolving in water to a 75% concentration. In addition to cesium, we have also used Rb, K, Ba, and Ca.

To obtain the second coating material, thermolysis of a metal carbonyl in solution with a functional polymer has been used to produce a dispersion of stable metal colloids in the polymer solution.[5] Colloid particle sizes range from 10 to 1000 Å. Smith and Wychick[6] have reported metal colloids of diameter 60–80 Å uniformly dispersed in styrene-butadiene copolymer. A sample of Fe-colloid dispersion with styrene-butadiene copolymer in decalin was obtained from Smith and Wychick and contained 4.5 atomic percent Fe per polymer after evaporation of the solvent. Oxidation of the colloid particles changes the resulting structure significantly.[6] This can be avoided or minimized by carrying out the thermolysis in an inert-gas atmosphere. The colloidal particles embedded in the polymer matrix are protected against oxidation in air.

Coating Methods

Metal-doped polymer materials have been solution-coated onto stalk-mounted laser-fusion targets. To be suitable for laser-fusion targets, the coating must satisfy exacting geometrical requirements including thickness uniformity, surface smoothness, absolute thickness, and in this case metal-dispersion homogeneity.

Simple solution dipping of targets has proved successful for coating thicknesses less than 0.5 μm. Here a stalk-mounted glass microballoon was immersed into a metal-neutralized sulfonated-polystyrene solution or a decalin solution of Fe-colloid dispersion of styrene-butadiene copolymer. For proper solution wetting of the microballoon, 0.1% of a surfactant, Photoflow, was added to the solution. With the decalin solution of Fe-colloid dispersion of styrene-butadiene copolymer, the surfactant was not necessary. After immersion, the solution-coated glass microballoon was suspended in air. For the Fe-colloid solution, the suspension was performed in an Ar-atmosphere glove box to minimize oxidation of the colloids. After drying, a polymer film encapsulated the glass microballoon.

The wetting agent decreased the contact angle between the solution and the stalk, causing a nonuniform coating as shown in Fig. 29. This was minimized by immersing the microballoon into the solution until its top surface was level with the solution surface. The final coating thickness depends primarily on solution viscosity and concentration. This functional relationship is presently being studied.

As the glass microballoon is removed from the solution in the dip coating, the surface tension of the solution causes the layer to sag, resulting in a nonuniform coating. This becomes pronounced for coatings thicker than 0.5 μm. Gravitational effects also contribute to the nonuniform coating, since the solution can flow singificantly during the time required for solvent evaporation. Uniform coatings thicker than 0.5 μm can be obtained by applying a centering force to a sagged coating during solvent evaporation. Viscosity, density,
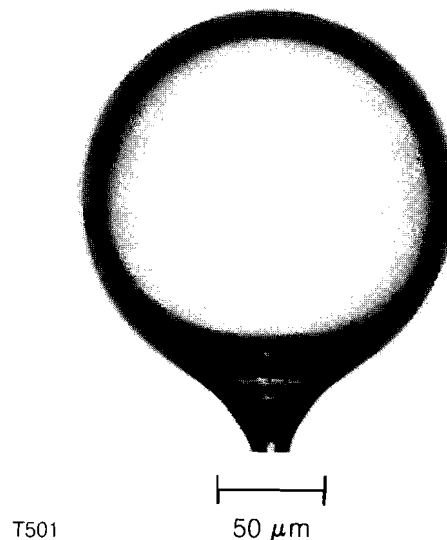
Fig. 29
Sulfonated-polystyrene Cs-salt coating produced by the dip method. The solution concentration was 40%, and the coating thickness was 14 μm. Notice the extra coating on the stalk due to surface tension.

T501   50 μm

coating thickness, and other factors of the solution determine the magnitude of the force required to form the concentric coating. This centering force can be produced by periodically inverting the target. A detailed study of this coating method is in progress, and preliminary results are very encouraging.

An alternative coating technique involves using an acoustic-levitation scheme. This method has previously been used to coat non-stalk-mounted levitated inertial-fusion targets with ablation layers. To coat a levitated microballoon, a glass microballoon is injected into an acoustic force field and trapped in a potential well. Subsequently, a drop of polymer solution, injected into the acoustic force field with a liquid atomizer, concentrically coats the glass microballoon. The solvent evaporates, leaving the microballoon coated with the polymer. In using acoustic levitation for coating a stalk-mounted balloon, the balloon was positioned in a stationary location. However, perturbations in the acoustic field caused a shift of the center of the acoustic potential well relative to the center of the microballoon, necessitating constant manual position adjustment.

Results and Discussion
The results of the present study are evaluated in terms of the coating requirements previously mentioned. Some coating properties, such as surface finish and homogeneity of the metal dispersion, are primarily functions of the materials utilized. Other properties, such as coating uniformity and thickness, depend strongly on the viscosity and concentration and, therefore, on the coating technique.

The typical surface structure of sulfonated-polystyrene coatings, as observed by Scanning Electron Microscopy (SEM), is shown in Fig. 30. The surface is extremely smooth and completely featureless. Similar surface smoothness was obtained with styrene-butadiene copolymer containing metal-colloid dispersions in the polymer matrix. Smooth surfaces are characteristic of non-
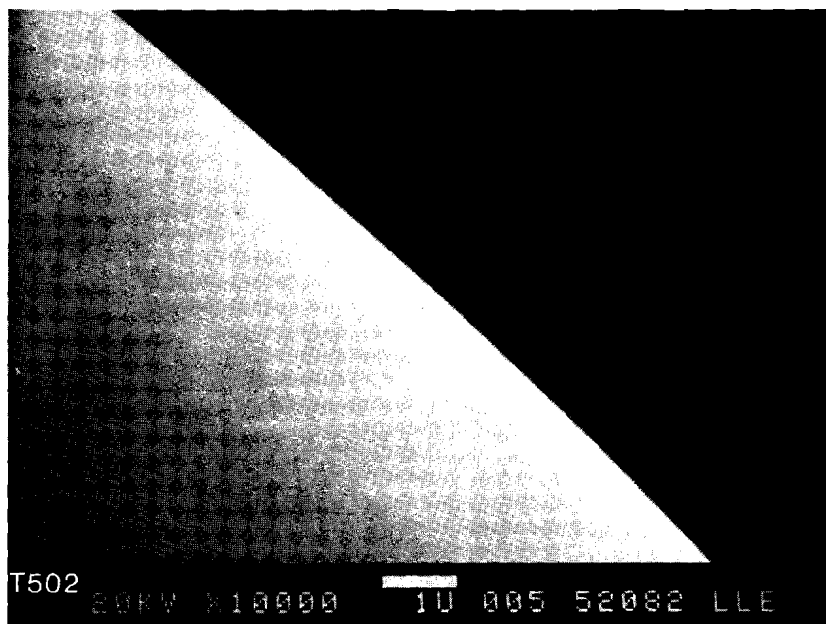
Fig. 30
Scanning electron micrograph of the surface of a sulfonated-polystyrene Cs-salt coating.

crystalline polymer-solution coatings because surface tension is the primary force forming the surface. This is in contrast with crystalline polymer-solution coating and vacuum-deposition methods. The surfaces of crystalline polymers frequently show crystal facets, and substrate defects are substantially amplified with vacuum-deposition methods, such as parylene coating or plasma polymerization. This results in cone defects or a wrinkled surface resembling "orange peel".

Most of the published work[7,8] on the morphology and structure of sulfonated polystyrene involves lightly sulfonated polystyrene (sulfonation level less than 8 mole percent). The state of ionic aggregation has not been completely elucidated in this polymer, but it is generally believed[9] that above a critical ion concentration of ca. 3 mole percent, ion-rich aggregates or clusters are formed, while below this critical concentration, ionic species are homogeneously dispersed. There is, however, no work reported on the structure of ionic aggregates of fully sulfonated polystyrene. Because of the very close ion proximity in the fully sulfonated polystyrene, a phase separation of ion-rich aggregates is extremely unlikely. In other words, metal atoms are expected to be homogeneously dispersed in the polystyrene matrix on the molecular scale.

With the metal-colloid-seeded polymers, metals are not dispersed homogeneously but phase-separated into colloids. We have not investigated the size of Fe colloids in a styrene-butadiene copolymer matrix, but it has been reported[5] that the size of Fe colloids is about 50 Å. Dispersion of these colloids may not be homogeneous on a molecular scale. Since any transition-metal carbonyl can be reduced to metal colloids, this method provides a broader range of average Z than does the sulfonation method.

45

Concentricity of thick coatings was investigated by contact x-ray radiography. For coatings with thicknesses less than 0.5 μm, simple solution dipping provided sufficiently concentric coatings. However, for thicker coatings, satisfactory concentricity was obtained only when performed with acoustic levitation. Figure 31 shows a contact x-ray radiograph of a glass microballoon coated with Cs-neutralized sulfonated polystyrene in an acoustic-levitation apparatus. A detailed description of the acoustic-levitation coating process is presented elsewhere.[10] From Fig. 31, the non-concentricity, defined as the difference between the thickest and the thinnest coatings divided by the average coating thickness, is calculated to be 0.08. Coating concentricity by acoustic levitation can be improved[10] using an automated position-adjustment system to center the microballoon in the liquid polymer layer. The Fe-colloid-seeded styrene-butadiene copolymer gave results similar to Fig. 31.
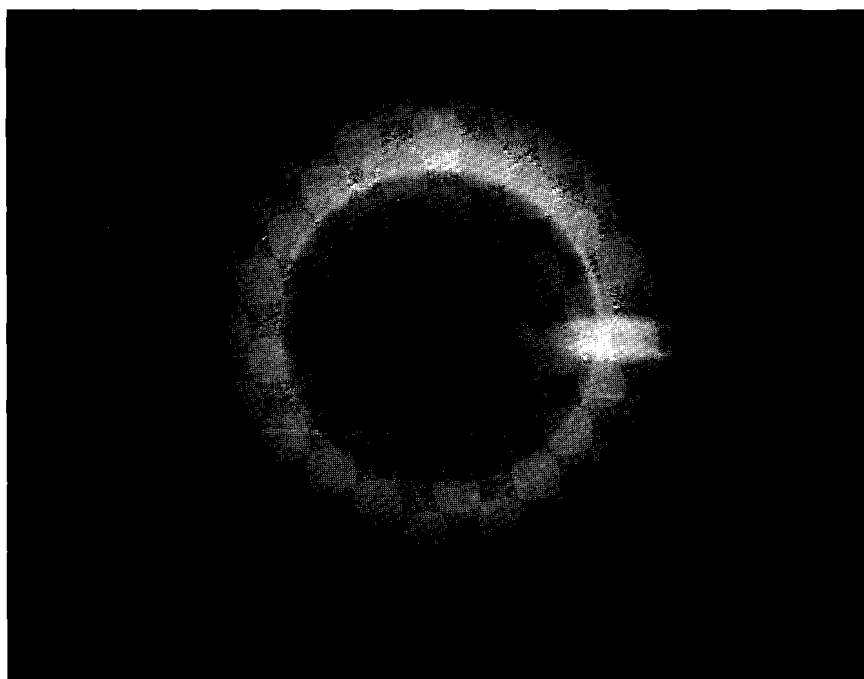

|————————|
50 μm

Fig. 31   T503
Contact radiograph of a sulfonated-
polystyrene Cs-salt coating on a glass
microballoon, produced by the acoustic-
levitation scheme.

In vacuum-deposition methods, particularly the parylene-coating method, real-time monitoring and control of coating thickness are possible using a laser reflectometer, and control of coating thickness to several hundred angstroms has been demonstrated.[11] In the solution techniques described in the present work, precise control of the thickness has not been achieved. The coating thickness depends on the viscosity and concentration of the solution, and the relationships are presently being studied.

Summary
Two polymer materials loaded with high-Z elements, and two

solution-coating techniques, have been investigated for fusion-target coating. Sulfonated polystyrene neutralized with various alkali and alkaline-earth metals has been coated onto glass microballoons by solution-dipping, and produced an atomic-scale dispersion of the metal in the polymer with an extremely smooth surface. This characteristic is usual for solution coating of non-crystalline polymers.

A metal-colloid-seeded polymer was also coated by solution dipping. Although a homogeneous dispersion of metal was not achieved, metal colloids are dispersed as small particles of size ca. 50 Å. This techique has an advantage in that practically any metallic element can be used for the colloid, thus providing a wider range of Z for the fabricated ablation layer.

ACKNOWLEDGEMENTS

REFERENCES

1. R. C. Kirkpatrick, C. C. Cremer, L. C. Madsen, M. M. Rogers, and R. S. Cooper, *Nucl. Fusion* **15**, 333 (1975).

2. M. C. Lee and I. Feng, *Rev. Sci. Instrum.* **53**, 854 (1982).

3. M. C. Lee, I. Feng, D. D. Elleman, T. G. Wang, and A. T. Young, *J. Vac. Sci. Technol.* **20**, 1123 (1982).

4. National Starch and Chemical Corporation, Chemical Products Brochure, VERSA-TL 121, Box 6500, Bridgewater, NJ 08807.

5. C. H. Griffiths, M. P. O'Horo, and T. W. Smith, *J. Appl. Phys.* **50**, 7108 (1979).

6. T. W. Smith and D. Wychick, *J. Phys. Chem.* **84**, 1621 (1980).

7. A. Eisenberg and M. King, *Ion-Containing Polymers: Physical Properties and Structure* (Academic, New York, 1977).

8. W. J. MacKnight and T. R. Earnest, Jr., *J. Polym. Sci., Macromol. Rev.* **16**, 41 (1981).

9. D. G. Peiffer, R. A. Weiss, and R. D. Lundberg, *J. Polym. Sci., Polym. Phys. Ed.* **20**, 1503 (1982).

10. M. C. Lee, I. Feng, T. G. Wang, and H. Kim, *J. Vac. Sci. Technol.*, to be published (1983).

11. H. Kim, T. F. Powers, and J. Mason, *J. Vac. Sci. Technol.* **21**, 900 (1982).

3.D   Real-Time Interactive Spectroscopy

In Sections 2.A and 2.B of this issue it is described how the spectroscopic analysis of light originating in the corona of laser-fusion targets provides information about important plasma processes. In particular, the 1/2-, 3/2-, 2-, and 5/2-harmonic multiples of the fundamental laser frequency ω_o have been spectrally resolved in experiments on OMEGA.

Earlier experimental work at LLE on harmonic emission by Rizzo et al.[1] and Tanaka et al.[2] involved recording information on film; subsequent film handling, and in the latter case digitizing, took several hours. Here we describe an alternative to film: we use an automated optical multichannel analyzer (OMA), which is capable of yielding quantitative spectroscopic measurements within a few seconds of a laser shot. This OMA-based system was used to obtain some of the data discussed in Section 2.A of this issue.

Early Work with OMA's at LLE

For several years the Laboratory has used OMA's manufactured by Princeton Applied Research (PAR). Our OMA's are silicon vidicons suitable for imaging infrared and visible light. Most recently, we have used a configuration consisting of an OMA, a controller and a computer for 2-D imaging of x-ray diffraction patterns,[3] imaging of streak cameras to temporally resolve laser pulses, and temporally resolving weak-fluorescence measurements.[4]

Two computer configurations have been employed. The first involves interfacing the OMA directly to a DEC LSI-11/23 computer, as used in Ref. 3. The second uses a packaged system from PAR called the OMA II, consisting of a DEC LSI-11 computer, memory-mapped graphics, and a direct-memory controller for up to four OMA's. As with many of our real-time automated diagnostics, this system was written in the Forth programming language.[5-7]

A recent application involved monitoring the lasing wavelength of the phosphate-glass oscillator on GDL. It was found that this wavelength could change under certain conditions when the oscillator was being serviced, thus significantly affecting the third-harmonic conversion efficiency of the GDL system. For this purpose the streak-camera acquisition and reduction system was modified to monitor instead a one-meter spectrometer with an overall spectral resolution of 1 Å. Although the dynamic range of the OMA was less than that of film, it was sufficient for this application. Using additionally an OMA-equipped streak camera, we are thus able to measure simultaneously the spectral and temporal shape of each oscillator pulse.

Harmonic-Emission Spectroscopy on OMEGA

This rapid turnaround of quantitative spectral information was seen as an advantage for the OMEGA coronal-physics experiments which began in early 1983. An OMA was therefore installed

on OMEGA, with the OMA head positioned at the output plane of a spectrometer as shown in Fig. 32. The OMA-head controller was connected by cable to a computer located in the control room. Noise arising from the electromagnetic pulse generated by target disassembly contributed fewer than 40 OMA counts to a background of about 2,000 counts; for comparison, typical data had up to 10,000 counts. The OMA was spectrally calibrated using a Cd lamp for $3\omega_0/2$ and a Th lamp for $5\omega_0/2$. Changes in spectrometer alignment were corrected using stored reference spectra.
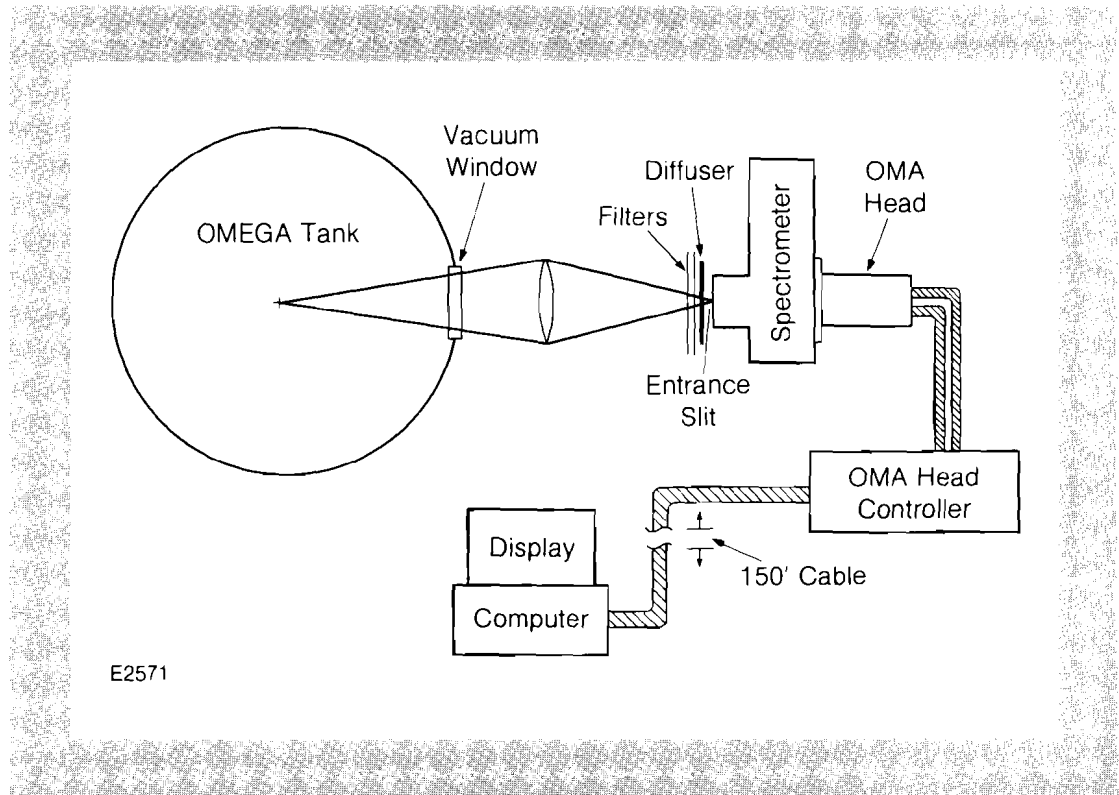

E2571

Fig. 32
Typical instrumentation configuration including the target chamber, spectrometer, OMA head and controller, computer and console.

Raw data was displayed on the OMA graphics screen immediately after each shot. A $3\omega_0/2$ spectrum taken at low intensity is shown in Fig. 33a, after background subtraction. The spectrum was then fitted using a third-order polynomial routine to yield the smooth curve of Fig. 33b. Even though the spectrum after background subtraction is dominated by noise, the resulting spectrum (Fig. 33b) clearly reveals the double-peaked structure characteristic of $3\omega_0/2$ spectra; for comparison, a more typical $3\omega_0/2$ spectrum is shown in Fig. 34. The computer system identified the various peaks by wavelength (see Fig. 34), and the scaled and labeled spectrum was plotted on an analog plotter. The system contained several interactive features; for example, data from two different shots could be superimposed and shifted with respect to wavelength; this was useful for identifying structural changes such as frequency shifting, broadening, and line splitting. A total of 120 spectra were recorded using the OMA in the course of the OMEGA coronal experiments, along with reference and background spectra.
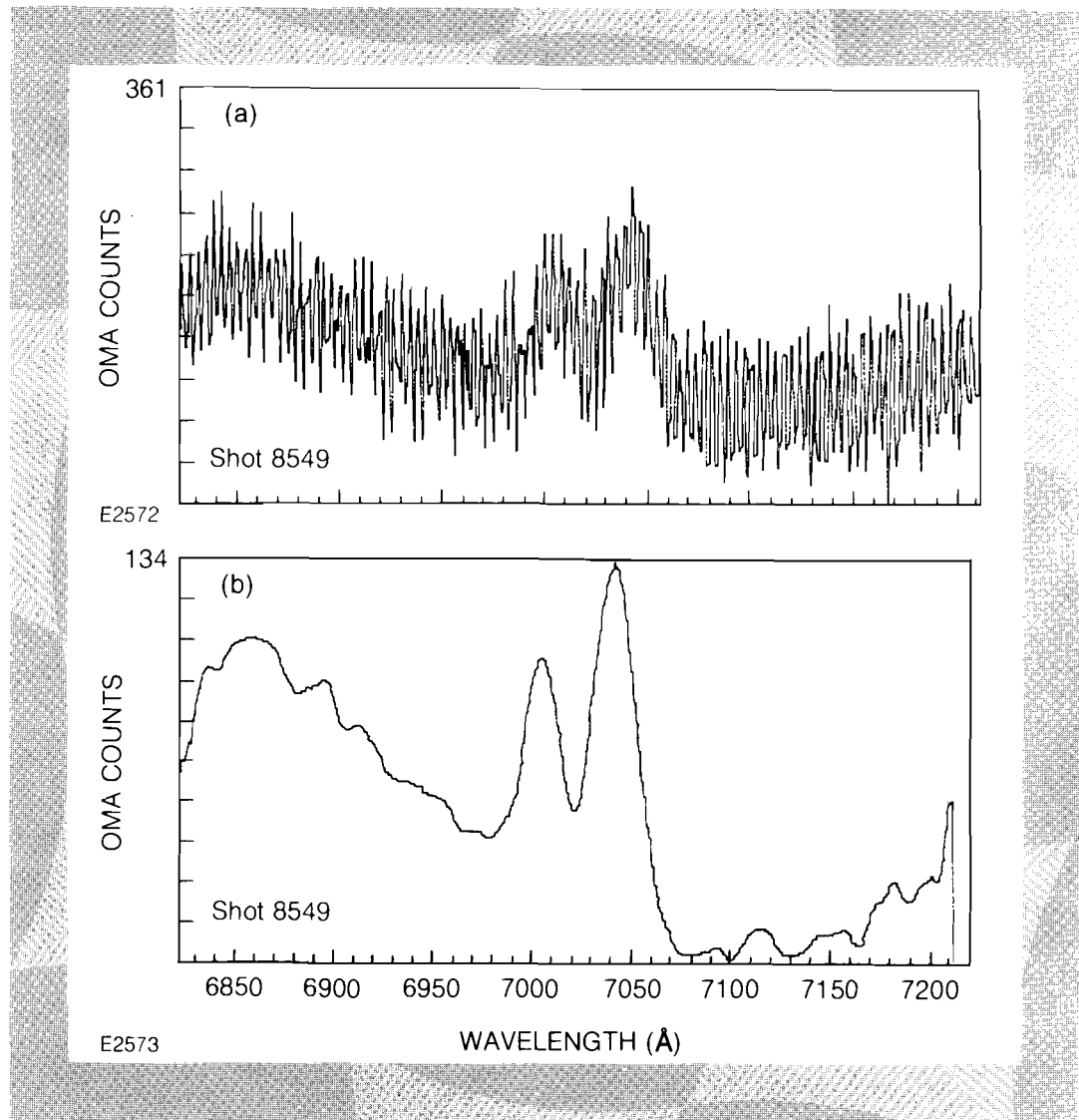
Fig. 33
Removal of noise from data. In this shot the signal on the spectrometer was attenuated to about 1% of normal, but the distinctive double-peaked $3\omega_o/2$ spectrum was extracted.

a) raw data after background subtraction.

b) after smoothing with a third-order-polynomial routine.

The flexibility and tradeoffs with regard to film become most apparent in Fig. 35, where $2\omega_o$ spectra taken on similar shots with the OMA and with film are compared. In comparison with film data, the OMA is seen to have a dynamic range of more than 100 (for these light pulses of nanosecond duration). Although many of the smaller peaks on these shots were lost with the OMA, the data were available less than 30 seconds after the shot, whereas data from film were not normally available until the following day. Clearly, the two approaches can complement one another.

Summary

Real-time interactive spectroscopy has evolved from automated systems developed to acquire and reduce streak-camera data. The flexibility of the silicon vidicon, the controllers, and the Forth-based software have allowed successive adaptations to very different experiments. Thus, we now have a system which complements the use of film in spectroscopy, allowing us to
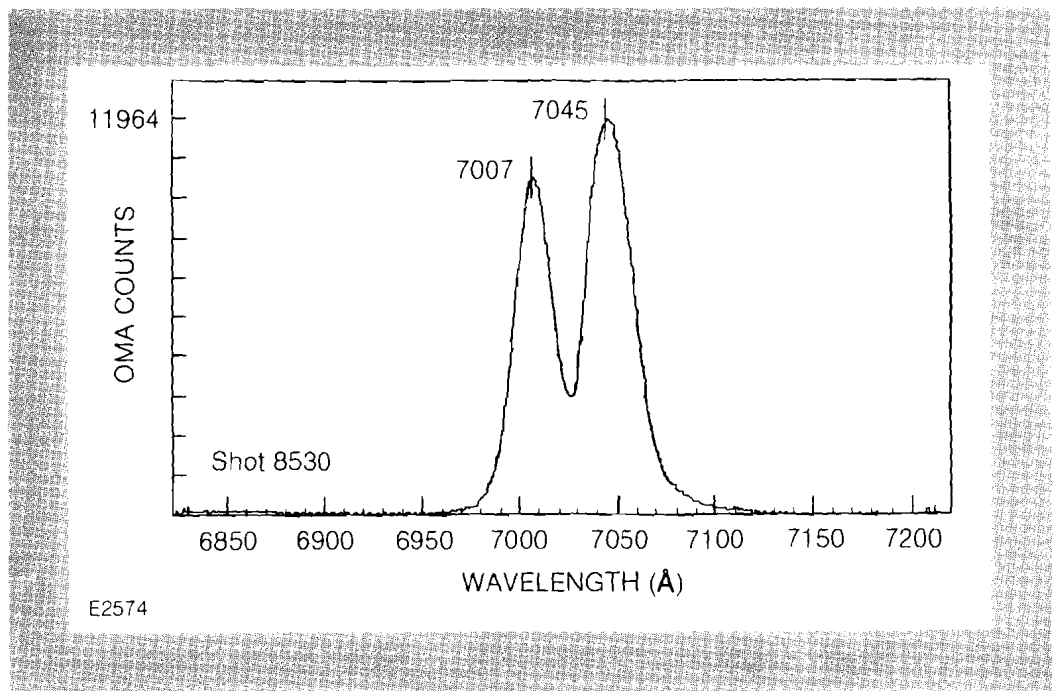
Fig. 34
Typical $3\omega_0/2$ spectrum from an OMEGA coronal-physics experiment, as obtained within a few seconds of the shot.

collect, reduce, and present data in a few seconds rather than after several hours. Although the reduced dynamic range and spatial resolution of our detector could in some circumstances be a disadvantage as compared with film, the rapid turnaround of data allows a tuning of experiments from shot to shot not otherwise possible.

REFERENCES

1. J. Rizzo, S. Letzring, D. Villeneuve, M. C. Richardson, G. Gregory, R. S. Craxton, J. Delettrez, K. Lee, and R. Hutchison, *Proceedings of the Second Conference on Lasers and Electro-Optics (CLEO),* Phoenix, AZ (1982).

2. K. Tanaka, L. M. Goldman, W. Seka, M. C. Richardson, J. M. Soures, and E. A. Williams, *Phys. Rev. Lett.* **48,** 1179 (1982). See also Section 2.A of this issue.

3. LLE Review **8,** 17 (1981).

4. W. Knox and L. Forsley, "Data Acquisition for a Jitter-Free Streak Camera," submitted to the American Chemical Society, Symposium on Multichannel Detectors.

5. J. Boles, D. Pessel, and L. Forsley, *IEEE J. Quantum. Electron.* **QE-17,** 1903 (1981).

6. Princeton Applied Research, Inc., Princeton, NJ, OMA II Open System Programming Manual.

7. C. Moore and E. Rather, *Proc. IEEE* **61** (9), 1346 (1975).
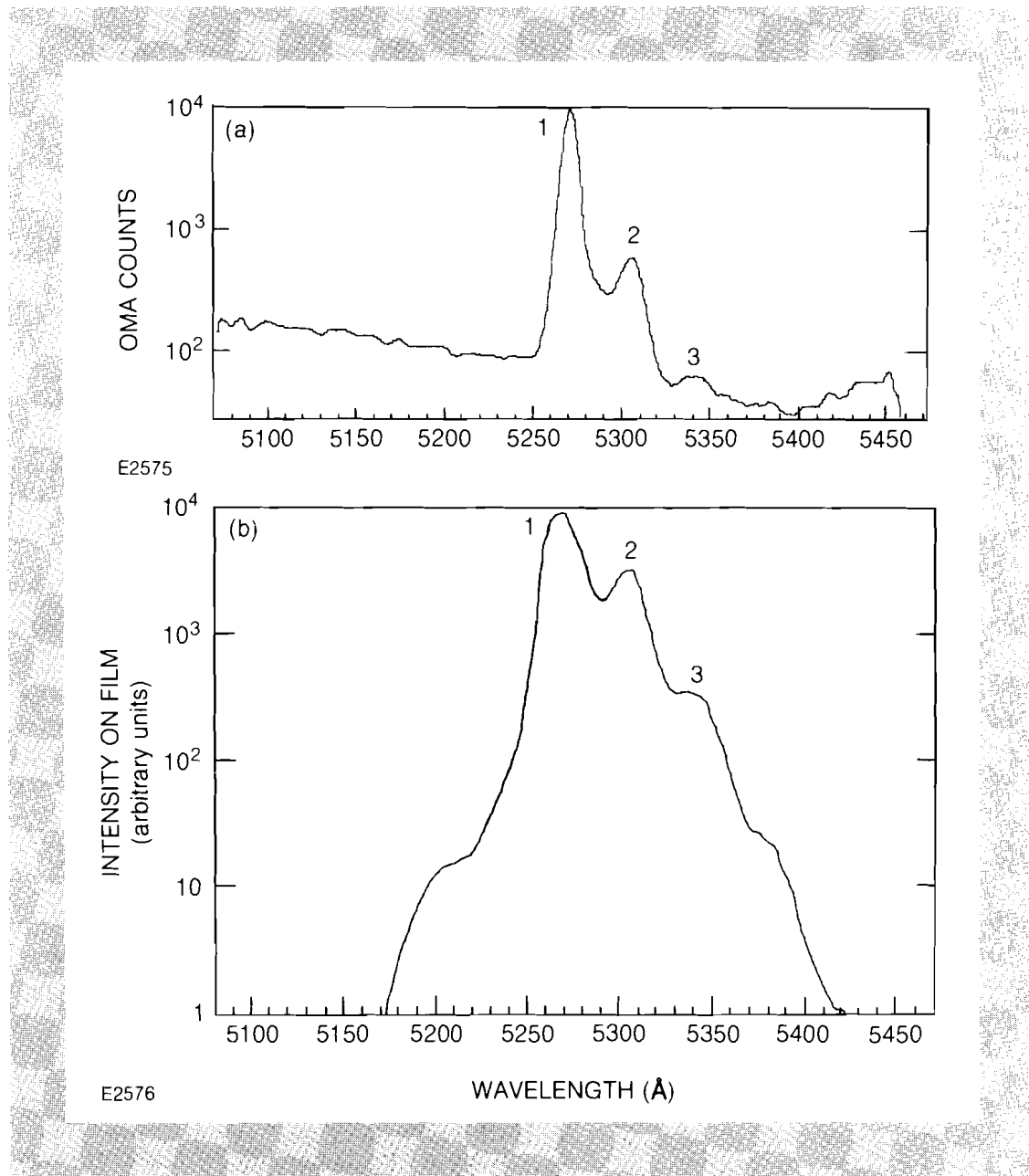
E2575

E2576

WAVELENGTH (Å)

Fig. 35
Comparison of the OMA- and film-collected $2\omega_0$ spectra:

a) Data taken with the OMA, using a logarithmic scale. Note peaks 1, 2, and 3.

b) Film-digitized spectrum from a similar shot with a logarithmic intensity scale. Note that there are resolvable peaks in addition to the three peaks found with the OMA, illustrating the higher dynamic range of film.

Section 4
NATIONAL LASER USERS FACILITY NEWS

This report covers the activities of the National Laser Users Facility (NLUF) during the quarter January to March 1983. During this period, eight users conducted experiments on LLE facilities. The visiting scientists associated with these experiments represented UCLA, Yale University, the Naval Research Laboratory, the University of Maryland, the University of Illinois, the University of Rochester, the University of Pennsylvania, and the University of Connecticut.

Eight user experiments were conducted in this quarter compiling a total of 118 shots on the Glass Development Laser (GDL) and the OMEGA laser system. Table 1 gives a summary of the number of shots for each user experiment.

Research scientists from the following institutions participated in the experiments:

1. Francis Chen, Chan Joshi, and Humberto Figueroa (UCLA), and Nizarali Ebrahim (Yale University).

2. J. Kent Blaise, D. Pierce, Donatella Pascolini, and A. Scarpa (University of Pennsylvania).

3. Leo Herbette and Robert McDaniel (University of Connecticut).

4. James Forsyth and Robert Frankel (University of Rochester).

5.   Uri Feldman and George Doschek (Naval Research Laboratory), Samuel Goldsmith (University of Maryland), and W. E. Behring (Goddard Space Flight Center).

6.   Hans Griem and Samuel Goldsmith (University of Maryland).

7.   George Miley, Chan Choi, Aaron Bennish, and David Harris (University of Illinois).

8.   Barukh Yaakobi (University of Rochester), and H. W. Schnopper and P. O. Taylor (Smithsonian Institution).

User System Shot Distribution
January 1 to March 31, 1983

USER (Principal Investigator)	FACILITY	NUMBER OF SHOTS
UCLA/Yale University (F. Chen)	GDL	26
University of Pennsylvania (J.K. Blaise)	GDL	28
University of Connecticut (L. Herbette)*	GDL	--
University of Rochester (J. Forsyth)	GDL	24
Naval Research Laboratory (U. Feldman)	OMEGA	18
University of Maryland (H. Griem)	OMEGA	15
University of Illinois (G. Miley)	OMEGA	5
University of Rochester (B. Yaakobi)**	OMEGA	2
	TOTAL	118

*Shared shots with the University of Pennsylvania
**Shared shots with other Users

U66

Table 1
User system shot distribution from
January 1 to March 31, 1983

This issue of the LLE Review highlights results from the University of Maryland experiment entitled "Shifts and Widths of Hydrogenic Ion Lines" (principal investigator, Hans Griem).

The experimental observation of shifts and widths of hydrogenic ion lines emitted by very dense plasmas is an essential step in the general study of the properties of bound states of multiply charged ions in dense plasmas. This research is of importance in a number of areas, notably equilibrium statistical mechanics (equation of state), plasma radiation physics (energy transport and diagnostics), and calibration of wavelengths in the extreme-vacuum-UV region ($10 \text{ Å} < \lambda < 200 \text{ Å}$). In the latter case, the

wavelengths of lines from one-electron ions are generally considered to be well known theoretically and are regarded as standards for plate calibration. The question nevertheless arises as to whether or not significant changes in wavelength can occur, for example in low-inductance sparks[1] or laser-produced plasmas[2] which are often used as line sources.

The existing theoretical treatments of the corresponding many-body problem include several proposed models, although no exact solutions are available. According to these models, the line width is due to plasma perturbation of the internal atomic electric field and depends on fluctuations in the local electric field. The line shift also depends on these fluctuations, but additionally depends on the value of the local plasma electron density. It should be noted that in the domain of high-density (compressed) laser-produced plasmas, the dominant parameter determining the line-shifts may be the mean value of the electron density, rather than the fluctuations. The opposite situation pertains to the more conventional domain of plasma spectroscopy, i.e., $N_e \sim 10^{17}\,cm^{-3}$ and $kT_e \lesssim 5\,eV$ where N_e is the electron density and T_e is the electron temperature.

The study of spectral line shifts and widths of hydrogenic ions reported here included the Lyman lines of CVI(C^{5+}), NVII(N^{6+}) and OVIII(O^{7+}) emitted by plasmas produced from microballoon targets by the 24 beams of the OMEGA laser system. Low-Z elements were chosen for this study because the wavelength shift scales as N_e/Z^6 (see Ref. 3). CVI and CV lines were produced either from solid polystyrene spheres or from shells of parylene-N coated on polystyrene supports. The sources of OVIII and OVII ions were either the oxygen component of the glass from the microballoons or oxygen gas inside the microballoons. Nitrogen was also used as a filling gas to obtain the lines of NVII.

The 24 laser beams were focused nearly tangential to the target spheres with the total energy $\approx 2.5\,kJ$, the pulse width in the range of 0.7 – 0.9 ns, and the radiation intensity $\approx 5 \times 10^{14}\,W/cm^2$. The spectrum was recorded with a 3-m grazing-incidence spectrograph[4] at an angle of incidence of 88°. The image of the point-like plasma source was focused onto the spectrograph slit using a cylindrical mirror fabricated from a Be strip (coated by high-Z elements) and bent to obtain a grazing-incidence reflection of the XUV radiation.[5]

In addition to the conventional photographic spectra, two runs were made with an additional 50-μm slit, placed perpendicular to the spectrograph slit, obtaining spatial resolution parallel to the direction of the main slit. This arrangement allowed us to record relative line shifts as functions of the distance from the center of the compressed plasma.

The spectra were calibrated using known lines of Si, Al, Ni, and Cu, which were introduced into the original target as metallic coatings. In Figs. 36 and 37 we present microdensitometer
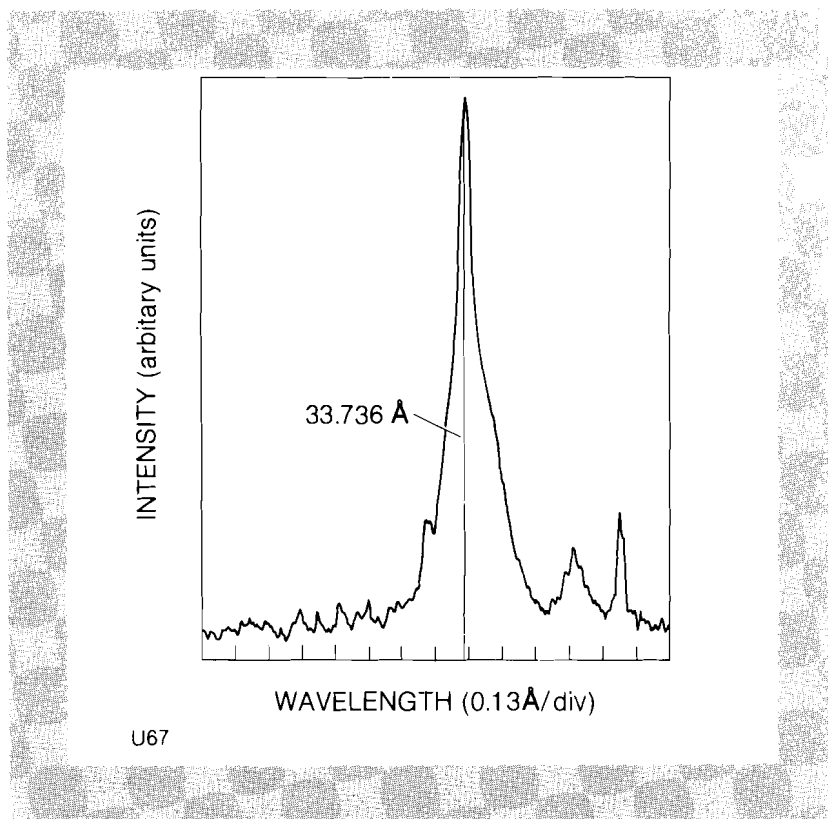
U67
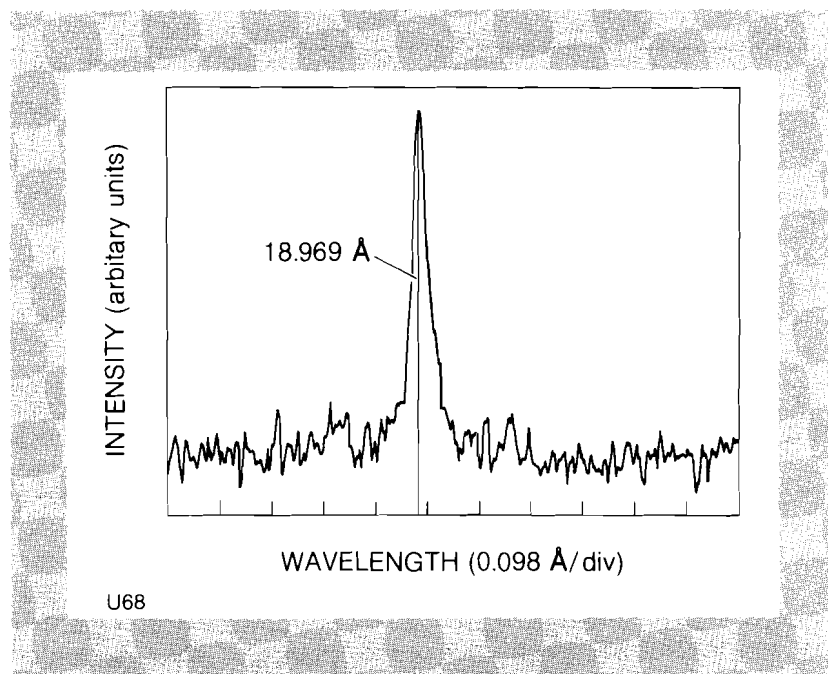
Fig. 36
The Lyman-α (L$_α$) line of CVI at 33.736 Å.

Fig. 37
The Lyman-α (L$_α$) line of OVIII at 18.969 Å

tracings of CVI and OVIII L$_α$ lines. The asymmetry of the lines is noticeable, there being an extended tail in the direction of longer wavelength. This L$_α$ shape can be explained, in part, as the effect of He-like lines of CV and OVII, arising from the simultaneous excitation of the two electrons in the He-like ions. However, it may

also be explained as the superposition of shifted and unshifted L_α lines.

A new and interesting result was obtained when a spatially resolved spectrum of the CVI L_α line was photographed. A two-dimensional microdensitometer tracing of this line is presented in Fig. 38. The horizontal direction corresponds to the wavelength λ, and the vertical direction gives spatial resolution. The arrow in Fig. 38 points toward a filament-like structure, protruding from the center of the line and indicating a change of wavelength with distance from the center. The maximum relative shift between the center of the broadened line and the extreme edge of the filament is about 80 mÅ. The dimension of the extended plasma is about 0.6 mm.

Fig. 38
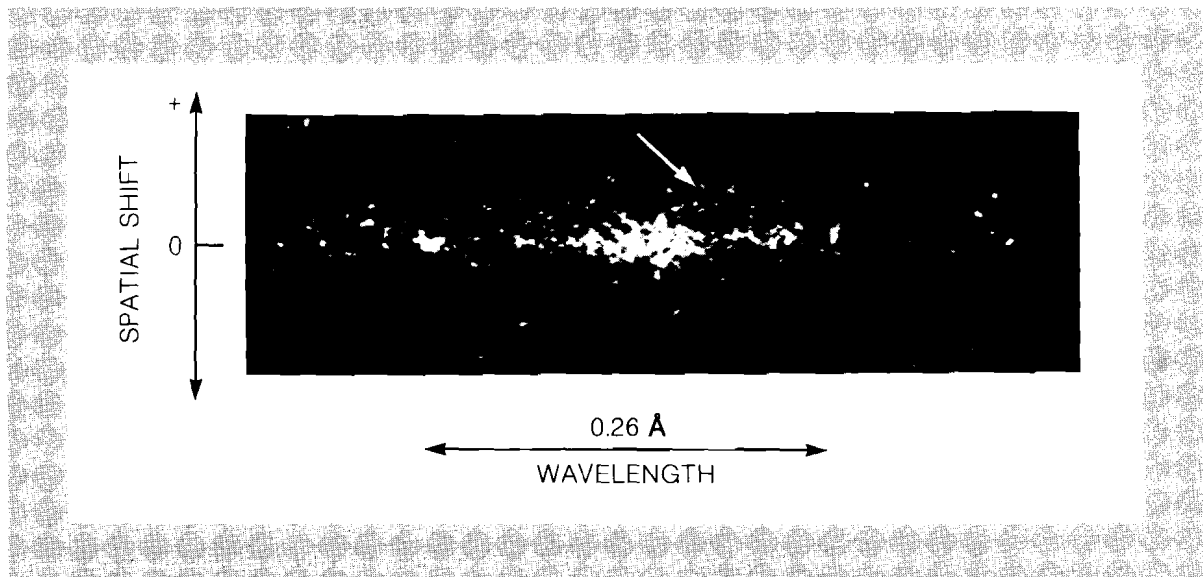Two-dimensional microdensitometer trace of the spatially resolved CVI L_α line. The horizontal axis corresponds to wavelength (λ increases to the right), and the vertical axis corresponds to spatial shifts from the line center (at zero).

It is too early to assess whether the plasma is so opaque and/or so highly ionized that the observed lines come mostly from a cool and not-so-dense region surrounding a hot plasma core. Furthermore, two additional effects, plasma motion and spectral satellites, should be considered; both of these may cause broadening and obscure shifts. The ratios of CV to CVI lines will also be studied with the data obtained here. From these ratios and from the broadening of the lines, the average values of N_e and T_e may be extracted. The next series of experiments will incorporate a second mirror for the spectrograph which will enhance the collecting power of the spectrograph and provide spatial resolution of the XUV emission.

Further information on the NLUF is available by writing to:

Thomas C. Bristow, Manager
National Laser Users Facility
Laboratory for Laser Energetics
University of Rochester
250 East River Road
Rochester, New York 14623

REFERENCES
1. B. Edlén, *Rep. Prog. Phys.* **26,** 181 (1963).

2. M. H. Key and R. J. Hutcheon, *Adv. A. Mol. Phys.* **16,** 201 (1980).

3. J. C. Adcock and H. R. Griem, *Phys. Rev. Lett.* **50,** 1369 (1983).

4. W. E. Behring, R. J. Ugiansky, and U. Feldman, *Appl. Opt.* **12,** 528 (1973).

5. J. H. Underwood, *Space Science Instrum.* **3,** 259 (1977).

PUBLICATIONS AND
CONFERENCE PRESENTATIONS

Publications

K. Lee, "Comments on 'Transverse Electromagnetic Waves with $\bar{E} \parallel \bar{B}$,'" *Phys. Rev. Lett.* **50**, 138-139 (1983).

M. C. Richardson, T. Boehly, R. S. Craxton, J. Delettrez, G. D. Enright, A. Entenberg, R. Epstein, W. Friedman, J. Hoose, R. Hutchison, S. Kacenjar, K. Lee, S. Letzring, R. S. Marjoribanks, R. L. McCrory, J. Rizzo, W. Seka, R. Short, S. Skupsky, J. M. Soures, C. Verdon, D. M. Villeneuve, E. A. Williams, and B. Yaakobi, "Direct-Drive Laser-Fusion Experiments with the OMEGA Laser System," *Plasma Physics and Controlled Nuclear Fusion Research 1982,* **1**, 477-485 (1983).

W. Seka, L. M. Goldman, M. C. Richardson, J. M. Soures, K. Tanaka, B. Yaakobi, R. S. Craxton, R. L. McCrory, R. Short, E. A. Williams, T. Boehly, R. Keck, and R. Boni, "Characteristics of UV-Laser-Matter Interaction," *Plasma Physics and Controlled Nuclear Fusion Research 1982,* **1**, 131-137 (1983).

Forthcoming Publications

T. Sizer II, J. D. Kafka, I. N. Duling III, C. W. Gabel, and G. A. Mourou, "Synchronous Amplification of Subpicosecond Pulses," accepted for publication by *IEEE Journal of Quantum Electronics.*

G. F. Albrecht, L. Lund, and D. Smith, "Building a Simple, Reliable, Low-Cost Modelocker System," accepted for publication by *Applied Optics.*

S. P. Sarraf, E. A. Williams, and L. M. Goldman, "Ion-Ion Two-Stream Instability in Multispecies Laser-Produced Plasma," accepted for publication by *Physical Review A: General Physics.*

J. Reynolds, "Information-Management Data Base for Fusion-Target Fabrication Processes," accepted for publication by *Journal of Vacuum Science and Technology.*

T. F. Powers and J. R. Miller, "Rotational-Shearing Interferometric Characterization of Inertial-Fusion Targets," accepted for publication by *Journal of Vacuum Science and Technology.*

H. Kim, J. Mason, and J. R. Miller, "High-Z-Doped Laser-Fusion-Target Ablation Layers Using Metal Colloids and Metal-Substituted-Sulfonated Polystyrene," accepted for publication by *Journal of Vacuum Science and Technology.*

D. Glocker, "Biased Magnetron Sputtering of ICF Target Pusher Layers," accepted for publication by *Journal of Vacuum Science and Technology.*

Conference Presentations

M. C. Richardson, "Critical Physics Issues for Direct-Drive Laser Fusion," presented at the Thirteenth Winter Colloquium on Quantum Electronics, Snowbird, Utah, January 1983.

R. D. Frankel, J. M. Forsyth, and B. K. Fung, "Time-Resolved X-Ray Diffraction Studies of Purple Membrane from Halobacterium Halobium," presented at the Biophysical Society Conference, San Diego, California, February 1983.

D. P. Butler, T. Y. Hsiang, and G. A. Mourou, "Transient Excitation and Restoration of Tin Micro-Bridges in the Presence of a Current Bias," presented at the American Physical Society Meeting, Los Angeles, California, March 1983.

D. R. Dykaar, C. V. Stancampiano, G. A. Mourou, and T. Y. Hsiang, "Experimental Determination of the Switching Threshold of a Super-Conducting Tunnel Junction," presented at the American Physical Society Meeting, Los Angeles, California, March 1983.

W. Lampeter and J. Wandtke, "Computerized Search of Chest Radiographs for Pulmonary Nodules," presented at the Thirty-First Annual Meeting, Association of University Radiologists, Birmingham, Alabama, March 1983.